AGU PUBLICATIONS

Water Resources Research

RESEARCH ARTICLE
10.1002/2016WR019480

Key Points:
- The effect of volcanic dykes on groundwater flow and solute transport is investigated using a field-scale multiphysics approach
- Ground magnetics, geoelectrics and tide-influenced groundwater monitoring data are used to calibrate a coastal aquifer numerical model
- Dykes hydrogeological properties are evaluated and are shown to result in preferential paths of flow and salt transport in the subsurface

Supporting Information:
- Supporting Information S1

Correspondence to:
J.-C. Comte,
jc.comte@abdn.ac.uk

Citation:
Comte, J.-C., C. Wilson, U. Ofterdinger, and A. González-Quirós (2017), Effect of volcanic dykes on coastal groundwater flow and saltwater intrusion: A field-scale multiphysics approach and parameter evaluation, *Water Resour. Res.*, *53*, 2171–2198, doi:10.1002/2016WR019480.

Received 10 JUL 2016
Accepted 19 FEB 2017
Accepted article online 23 FEB 2017
Published online 16 MAR 2017

Effect of volcanic dykes on coastal groundwater flow and saltwater intrusion: A field-scale multiphysics approach and parameter evaluation

J.-C. Comte[1], C. Wilson[2], U. Ofterdinger[3], and A. González-Quirós[4]

[1]School of Geosciences, University of Aberdeen, Aberdeen, UK, [2]Centre for Sustainable Technologies, School of the Built Environment, University of Ulster, Newtownabbey, UK, [3]School of Natural and Built Environment, Queen's University Belfast, Belfast, UK, [4]Hydrogeophysics and NDT Modelling Unit, University of Oviedo, Oviedo, Spain

Abstract Volcanic dykes are common discrete heterogeneities in aquifers; however, there is a lack of field examples of, and methodologies for, comprehensive in situ characterization of their properties with respect to groundwater flow and solute transport. We have applied an integrated multiphysics approach to quantify the effect of dolerite dykes on saltwater intrusion in a coastal sandstone aquifer. The approach involved ground geophysical imaging (passive magnetics and electrical resistivity tomography), well hydraulic testing, and tidal propagation analysis, which provided constraints on the geometry of the dyke network, the subsurface saltwater distribution, and the sandstone hydrodynamic properties and connectivity. A three-dimensional variable-density groundwater model coupled with a resistivity model was further calibrated using groundwater and geophysical observations. A good agreement of model simulations with tide-induced head fluctuations, geophysically derived pore water salinities, and measured apparent resistivities was obtained when dykes' hydraulic conductivity, storativity, and effective porosity are respectively about 3, 1, and 1 orders of magnitude lower than the host aquifer. The presence of the dykes results in barrier-like alterations of groundwater flow and saltwater intrusion. Preferential flow paths occur parallel to observed dyke orientations. Freshwater inflows from upland recharge areas concentrate on the land-facing side of the dykes and saltwater penetration is higher on their sea-facing side. This has major implications for managing groundwater resources in dyke-intruded aquifers, including in coastal and island regions and provides wider insights on preferential pathways of groundwater flow and transport in highly heterogeneous aquifer systems.

1. Introduction

In situ characterization of preferential pathways of groundwater flow and contaminant transport remains one of the greatest challenges in hydrogeology [e.g., *De Marsily et al*., 2005; *Dogan et al*., 2014]. Preferential groundwater pathways are primarily controlled by heterogeneity, discontinuity, and anisotropy of aquifer properties across different scales [e.g., *Berkowitz*, 2002; *Zheng and Gorelick*, 2003; *Neuman*, 2005]. In situ knowledge of these properties is crucial to develop and manage groundwater resources both quantitatively and qualitatively, through for example the application of numerical groundwater models. Among the range of groundwater contamination problems, there is a pressing need for improving the understanding of the influence of field/local scale aquifer heterogeneity (meters to hundreds of meters) on saltwater intrusion in coastal aquifers [e.g., *Simmons et al*., 2001; *Werner et al*., 2013]. In these coastal environments, the presence of intruding salt water provides a natural tracer which may be used to provide insights regarding preferential pathways and which in turn may be generalized to other dissolved contaminants in other non coastal, complex hydrogeological systems. Most research published to date on preferential flow and transport in highly heterogeneous aquifers has been focusing on fractured systems, karstic systems, or heterogeneous/anisotropic sedimentary systems [e.g., *Dogan et al*., 2014]. In situ, quantitative studies of the role of volcanic dykes on groundwater flow and contaminant transport at the field scale are lacking.

Volcanic dykes are very common geological discontinuities and have long been recognized as altering groundwater flow in aquifers [*Singhal and Gupta*, 1999; *Cook*, 2003; *Ernst*, 2014]. Fewer studies have looked at their effect on solute transport, including saltwater intrusion [e.g., *Souza and Voss*, 1987; *Izquierdo*, 2014].

Depending on the geological context, volcanic dykes have been described as constituting either draining structures or barriers to flow [*Custodio*, 2007; *Ernst*, 2014]. Draining features are typically observed in relatively low permeability, competent/hard rock environments. In these cases, the relatively high permeability is due to a high degree of dyke weathering and/or to the fracturing of the host rock during emplacement together with the contraction and internal fracturing of the volcanic material during cooling [*Singhal and Gupta*, 1999; *Bromley et al*., 1994; *Sami and Hughes*, 1996; *Wilkes et al*., 2004; *Vittecoq et al*., 2015]. In contrast, barrier features have been described for unweathered dykes emplaced in higher permeability and/or poorly consolidated host rocks [*Williams and Soroos*, 1973; *Takasaki and Mink*, 1985; *Engel et al*., 1987, 1989; *Lewis*, 1991; *Babiker and Gudmundsson*, 2004; *Perrin et al*., 2011]. This can be explained by the fact that in poorly consolidated rocks (1) the dyke contraction during cooling is accommodated by the sediment elasticity, therefore preventing the apparition of open space at the dyke borders and favoring porosity decrease through hydrothermal recrystallization in the contact zone [e.g., *Summer and Ayalon*, 1995] and/or (2) the permeability related to the dyke internal fractures/joins remains lower than those of the high-permeability host rock.

Despite an abundance of studies having mapped dykes occurrence in aquifers using methods such as field observations, remote sensing techniques or geophysical investigations [e.g., *Sultan et al*., 2008; *Dickson et al*., 2014, 2015], to our knowledge few studies have provided estimates of hydraulic properties of dykes, such as hydraulic conductivity and storativity. Moreover, their properties with respect to solute transport in groundwater such as saltwater intrusion are poorly documented despite their importance in many coastal settings, particularly volcanic islands. Examples of direct parameter evaluation include the works of *Boonstra and Boehmer* [1986], *Boehmer and Boonstra* [1987], and *Perrin et al*. [2011] who performed analysis of pump tests carried out within high-permeability dykes. These, however, constitute rare cases of test boreholes intersecting dykes on their entire depth of penetration. This is uncommon in practice due to the relatively small thickness of dykes (few meters) and their dipping angle which is rarely perfectly vertical. Instead, other numerous studies [*Williams and Soroos*, 1973; *Takasaki and Mink*, 1985; *Dickson et al*., 2014, 2015; *Izquierdo*, 2014] have given equivalent (upscaled) properties for dyke-intruded reservoirs or qualitative estimates of dyke role have been given by indirect observations such as evidence of barriers recorded on long-term pumping tests, spring lines, etc. and these studies did not consider solute transport. However, having quantitative estimates of flow and transport properties of dykes is necessary to perform numerical groundwater modeling at field or regional scales and further quantitative management of groundwater resources, particularly for settings where dykes are known to have a significant impact on groundwater flow and contaminant transport.

In the Sherwood sandstone aquifer of the Belfast region in Northern Ireland, the effects of basaltic dykes on groundwater flow and storage are long recognized and were first described by *Hartley* [1935]. Many studies since then have also mentioned detrimental effects of dykes on potential flow to wells through evidence of impervious limits during pump tests and evidence of relative compartmentalization of the aquifer from piezometric mapping [*Bennett*, 1976; *Robins*, 1996; *Kalin and Roberts*, 1997; *Cronin et al*., 2005]. Wells situated either side of a basalt dyke appear to have poor hydraulic connectivity, but wells within the same sandstone block appear to have excellent groundwater connectivity [*Earls and Young*, 2010]. This has been addressed as a groundwater management issue by others [*Cronin et al*., 2005; *Kalin and Roberts*, 1997] but no comprehensive study has conclusively quantified the impact of the dolerite dykes on the groundwater flow in the aquifer. In particular, no published work has attempted to assess the hydraulic properties of the dykes which remain unknown until recent works. The TELLUS regional airborne geophysical survey of Northern Ireland provided comprehensive magnetic mapping highlighting the dykes and dyke swarms at the regional aquifer scale [*Chacksfield*, 2010; *Young*, 2016]. A detailed geological interpretation of the Northern Ireland data set is presented by *Cooper et al*. [2012]. This data set has provided the opportunity to revise existing regional groundwater models incorporating the mapped dykes [*Dickson et al*., 2014, 2015].

In their recent review, *Werner et al*. [2013] have highlighted the need for more field research on the influence of aquifer heterogeneity on saltwater intrusion in coastal aquifers. Ground geophysical methods are efficient to characterize aquifer heterogeneity. Passive magnetics is a well-established technique for characterizing the 3-D structure of magnetized volcanic dykes [e.g., *Parasnis*, 2012, and references therein] but do not inform on groundwater salinity. Geoelectrical methods, particularly electrical resistivity tomography (ERT), are efficient for mapping complex saltwater distribution in aquifers [e.g., *Abdul Nassir et al*., 2000;

Attwa et al., 2011; *Bourhane et al*., 2016], more so when combined with groundwater model simulations, which further enables quantification of associated flow and transport and parameter calibration [*Comte and Banton*, 2007; *Koukadaki et al*., 2007; *Nguyen et al*., 2009; *Comte et al*., 2010, 2014; *Carrera et al*., 2010; *Beaujean et al*., 2014, *Van Dam et al*., 2014].

Airborne geophysical techniques are also increasingly used for hydrogeological investigations and modeling, including in heterogeneous volcanic environments [e.g., *Kirkegaard et al*., 2011; *Dickson et al*. 2014, 2015; *Vittecoq et al*. 2014, 2015]. They provide valuable data sets to elucidate regional or catchment scale structural controls on groundwater flow but lack sufficient spatial resolution for imaging field (local) scale groundwater processes such as complex 3-D flow and saltwater intrusion patterns induced by field heterogeneities (e.g., fractures and dykes).

This research presents direct, in situ experimental testing and modeling at field scale (hundreds of meters) aiming to quantify the hydrogeological properties of a complex dyke network within a coastal aquifer and its impact on groundwater flow and saltwater intrusion. A multiphysics approach was applied to characterize the dyke network structure, the saltwater distribution patterns and the properties of the host aquifer using high resolution ground geophysical investigations and modeling (ERT and passive magnetics), borehole hydraulic testing (pumping and recovery tests) and temporal analysis of the propagation of the tidal fluctuations (Ferris-Jacob model). Field data were subsequently integrated within a numerical groundwater flow and transport model coupled with a forward resistivity model to constrain and quantify the hydraulic properties of the dykes. The results provide valuable data and generalizable insights on preferential flow and transport patterns in productive aquifers intersected by complex distributions of discrete low-permeability geological features.

2. Site Selection and Hydrogeological Setting

The Sherwood sandstone aquifer beneath the Lagan river valley and Belfast is composed of moderately consolidated Permo-Triassic clay-sands reaching up to 300 m thickness [*Mitchell*, 2004]. The Sherwood sandstone aquifer displays hydraulic conductivity values ranging from 1×10^{-7} to 7×10^{-5} m s^{-1} with most typical values between 4×10^{-6} and 5×10^{-5} m s^{-1} [*Bennett*, 1976; *Robins*, 1996; *Kalin and Roberts*, 1997; *Yang et al*., 2004]. Typical transmissivity is around 1.5×10^{-3} m^2 s^{-1}, storativity around 2×10^{-3} [*Bennett*, 1976; *Kalin and Roberts*, 1997; *McNeill et al*., 2000] reflecting broad semiconfined conditions and porosity is approximately 0.1–0.2 [*Robins*, 1996; *McKinley et al*., 2001]. It is considered as a moderately productive aquifer, but of great economic importance to the region providing water supply for agriculture, heavy industrial processes, and the bottled drinks industry [*Kalin and Roberts*, 1997]. Toward the end of the last century, abstraction from the aquifer has been dominated by public supply boreholes (extracting 3,000–10,000 m^3d^{-1}) with an increasing number of industries utilizing the resource [*McNeill et al*., 2000]. The aquifer is classified as highly vulnerable to groundwater pollution owing to the permeability of the Sherwood Sandstone Group and the variable pollution attenuation capacity of the unsaturated zone [*Robins*, 1996; *Ball et al*., 2005]. Therefore, protection of the aquifer from both diffuse and point source pollution is of major importance. The necessity to develop appropriate groundwater management strategies is acknowledged by the *European Commission* [2006] requiring protection of groundwater from all contamination, and abstraction limits which maintain the sustainability of the resource. As a result there is a requirement to ensure that the aquifer is hydraulically understood in order to permit the development of source protection zones and a more complete management of the groundwater resource.

The TELLUS regional airborne geophysical survey of Northern Ireland [*Chacksfield*, 2010; *Cooper et al*., 2012] has emphasized the complexity of dyke clustering present in the Sherwood sandstone aquifer. In order to test the hydraulic and hydrogeological impacts of the dyke clustering on groundwater flow in the Sherwood sandstone aquifer a suitable site was identified north of Belfast, at Whiteabbey, situated on the coast of Belfast Lough, where outcropping dykes are clearly visible in aerial imagery (Figure 1). The site provided the opportunity for a variety of characterization and investigative techniques to be implemented benefiting from a predictable fluctuating tidal boundary (Belfast Lough), enabling both groundwater flow and saltwater distribution and transport to be monitored and modeled relative to the tides.

At the site, the beach and gardens are divided by a pedestrian promenade and 1–2 m of rock armor. The upper regions of the beach consist of fine sand translating to outcropping sandstone with visible dyke

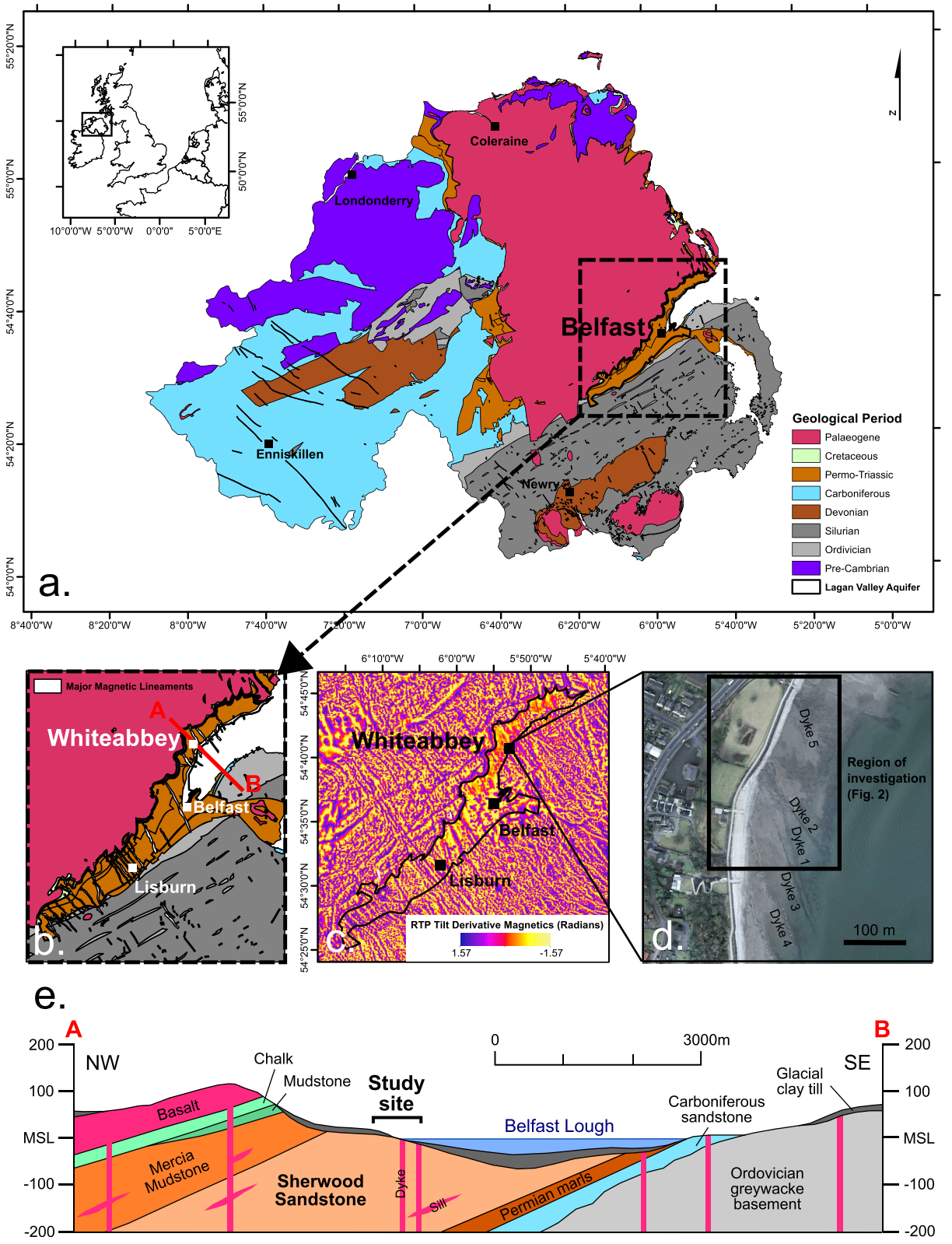

Figure 1. Location of the study site: (a) geological setting of Northern Ireland with location of the Lagan Valley sandstone aquifer, (b) detailed view of the geology of the Lagan valley with location of major magnetic lineaments from the interpretation of airborne magnetic maps, (c) tilt derivative transformation of airborne magnetic map highlighting magnetic lineaments related to volcanic dyke swarms, (d) Google Earth aerial photo of the Whiteabbey site showing individual dykes outcropping in the tidal flat, and (e) diagrammatic geological cross sections across Belfast Lough (adapted from *Robins* [1996]); dykes are represented as perpendicular to the cross section but are in reality subparallel to it.

intrusions ranging in thickness of approximately 0.5–2 m. Regions of contact metamorphism of the host rock are evident on the margins of the dykes, resulting in a slightly recrystallized metaquartzite [*McKinley et al*., 2001]. The Sherwood sandstone is estimated to be about 200 m thick at the site (Figure 1e).

3. Methodology

An integrative multiphysics methodology was developed, that combines geophysical investigations and hydrogeological time-series analyses to constrain a numerical groundwater model ultimately applied to assess the hydraulic properties of volcanic dykes and their effect on groundwater flow and saltwater intrusion. Passive magnetic mapping was used to delineate dykes and to model their dipping angle. Electrical resistivity tomography was used to both assess the relative compartmentalization of the sandstone aquifer and image the influence of the dykes on saltwater intrusion. A number of piezometers were installed within different dyke-bounded blocks of the sandstone host rock and hydraulic tests were carried out to estimate the local hydraulic properties of the sandstone. Groundwater was also monitored in piezometers and tidal attenuation techniques were applied to provide initial qualitative insights on the hydrodynamic role of dykes. Finally, a numerical groundwater model integrated all acquired geophysical and hydrogeological data and was used to quantify the hydrodynamic properties of the volcanic dykes through manual trial-and-error calibration to multiphysical observation data.

3.1. Geophysical Investigations

Initial geophysical investigations (passive magnetics) aimed to characterize the extension and dip of outcropping coastal dykes landward as they disappear under till cover. Further geophysical profiling electrical resistivity tomography (ERT) aimed to confirm the geology of the site and characterize the salt water intrusion relative to the dyke geometries.

3.1.1. Passive Magnetics Surveys

Measurement of the spatial variations of the geomagnetic field on the site was carried out using a proton magnetometer (Geometrics G-816). The magnetic susceptibility of both the dykes and host sandstone was also measured at 9.0 and 0.2 SI respectively on the outcrops of the tidal flat (Figure 2). To further assess the dip and extension of the dykes with depth, forward 3-D magnetic modeling was performed using the code *MAG3D* [2006] v4.0 from UBC-Geophysical Inversion Facility. The magnetic maps were not reduced to pole as the regional geomagnetic field properties were ultimately accounted for in the forward modeling.

3.1.2. Electrical Resistivity Tomography (ERT)

Geology and salt water distribution in the aquifer at the study site were characterized through 2-D electrical resistivity tomography (ERT) implemented on transects both perpendicular (ERT1, total length 145 m) and parallel to the shore (ERT2, total length 225 m) (Figure 2). Apparent resistivity measurements were acquired using a Syscal Pro-Switch 72 resistivity meter (Iris Instruments), a dipole-dipole array configuration and a unit electrode spacing of 2.5 m. Data for ERT1 ($n = 1529$) and ERT2 ($n = 3099$) were inverted with the BERT code [*Günther et al*., 2006; *Rücker et al*., 2006], which uses a 2-D unstructured triangular finite element mesh and an iterative least square (L_2-norm) algorithm. The DOI (depth of investigation) analysis of *Oldenburg and Li* [1999] was applied to the inversion results in order to identify model domains that are insufficiently constrained by the measured data, i.e., conventionally when DOI > 0.1.

3.2. Groundwater Monitoring

3.2.1. Monitoring Infrastructure

Data from the geophysical survey, providing information on dyke geometry and lithology, were used to site the installation of shallow piezometers and boreholes. The rationale for siting the wells was twofold: (1) to observe groundwater fluctuations in areas where dykes are likely to affect groundwater flows and conversely in areas where they will not and (2) to observe groundwater flows at varying distances from the shore.

Boreholes were completed on land above the highest tides, down to depths ranging 2.7–4 m below ground level (Table 1 and Figure 2; see also the technical details of the borehole and piezometers in Supporting Information S1). Drilling of the wells encountered sandstone at relatively shallow depths between 1 and 2.4 m. The sandstone is overlain by glacial clay till with some wells encountering thin layers of alluvial sands and gravels. Sediments overlying the Sherwood sandstone thin toward the shore (Figure 1). Groundwater strikes were recorded in the upper regions of the sandstone. A line of wells pz8, pz2 (within a dyke-

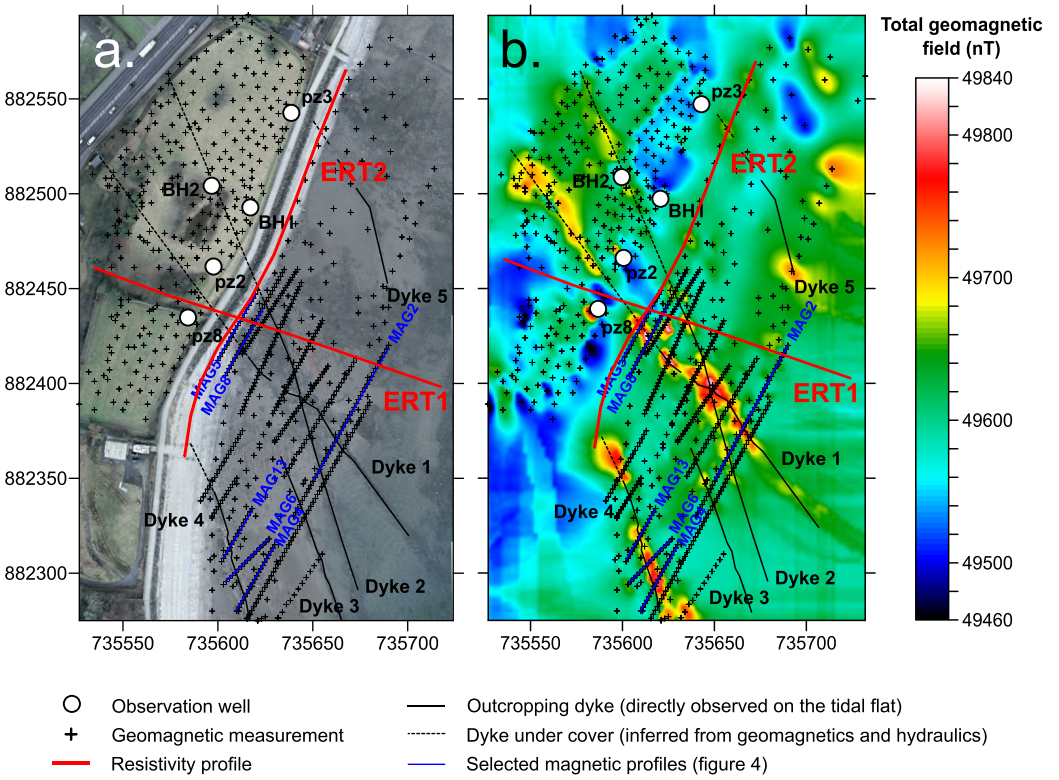

Figure 2. Maps of the study site showing the well locations, the magnetic measurements (including coarse grid and refined transects both indicated by small black plus symbol), the selected magnetic profiles (Figure 4) and the resistivity profiles on both (a) aerial photo and (b) interpolated magnetic map. The locations of volcanic dykes are obtained from outcrop observation (Figure 2a) and magnetic interpretations (Figure 2b). Latitude/longitude coordinates in meters.

bounded block), BH1, and pz3 were placed approximately equidistant from the high tide shoreline (as defined previously). Well BH2 was placed further inland from the shoreline.

3.2.2. Groundwater Levels

The observation wells were instrumented using Solinst leveloggers for the larger diameter boreholes (prefixed BH, Figure 2) and Schlumberger minidivers for the smaller diameter piezometers (prefixed pz, Figure 2). The atmospheric pressure was also recorded using a dedicated barologger (Schlumberger barodiver) in order to perform atmospheric compensation to recorded groundwater data. Top of well casing was measured using a differential GPS so that groundwater levels could be referenced to Belfast Lough mean sea level datum.

Groundwater levels in BH1 and BH2 were monitored at the site between 10 June 2011 and 10 August 2011. Wells pz2, pz3, and pz8 were not instrumented until 17 June. All wells were monitored at 10 min intervals.

Table 1. Hydrogeological Characteristics of Installed Piezometers (BGS = Below Ground Surface; AMSL = Above Mean Sea Level)

Well	Nearest Distance From Mean Tide[a] (m)	Depth to Sandstone[b] BGS (m)	Depth of Well BGS (m)	Well Elevation AMSL (m)	Observed Piezometric Level Range AMSL (m)	Aquifer Degree of Confinement
BH1	15	1.0	4.0	3.022	0.3–1.5	Unconfined
BH2	25	2.4[c]	4.0	3.617	1.7–2.5	Confined
Pz2	17	1.5	3.0	2.678	1.3–2.0	Confined
Pz3	12	1.0	2.7	2.722	0.6–1.6	Unconfined
Pz8	17	1.5	3.0	2.544	0.9–1.6	Semiconfined

[a]By definition the distance to the topographic contour 0 m AMSL.
[b]In all wells, the sandstone is overlain by clay till.
[c]BH2 was likely drilled in the baked contact zone of Dyke 2, as suggested by higher resistance to drilling, lighter sandstone color in the cuttings, and presence of dolerite debris.

3.3. Hydraulic Testing

Constant rate pump and recovery tests were performed in BH1 and BH2 (the largest diameter wells, see Supporting Information S1) and slug tests in pz2, pz3, and pz8 to obtain specific hydraulic parameters for the sandstones due to the impossibility to insert a submersible pump. Constant pump rates of 0.16 L/min for 200 min and 0.17 L/min for 61.5 min were used in BH1 and BH2 respectively with subsequent recovery being measured. Slug tests lasted 70.5 and 70 min in pz2 and pz8 respectively to recover the original static level, while pz3 returned to static much quicker lasting only 24 min.

Due to the low pump rate and the relatively shallow depth of the boreholes and piezometers, the derived parameters are representative of the near-well environment. The interpretation of the tests was done using the software AQTESOLV Pro (HydroSOLVE). The best fits were obtained with the *Moench* [1997] method for the pump and recovery tests and the *Bouwer and Rice* [1976] method for the slug tests. For the pumping and recovery tests, the *Moench* method was selected among the few methods that were suitable for the local aquifer typology, i.e., those that allow accounting for partially penetrating and semiconfined to unconfined conditions during pumping (the water table which is naturally fluctuating above and below the base of the confining clay till dropped below the confining layer during the tests). The best fit was obtained with the Moench solution, which accounts for an aquifer delayed gravity response consistent with the gradual drainage from an aquitard (i.e., the till) placed above the pumped unit [*Moench*, 1995, 1997], and possible wellbore storage due to large contrast of permeability between the gravel pack and the clay-sand aquifer.

3.4. Tidal Attenuation Analysis

The attenuation of the tidal signal of the Lough in the observation wells as predicted by the POLTIPS-3 software [*National Oceanography Centre*, 2011] was analyzed to provide additional estimates of the aquifer hydraulic properties using the analytical solution of *Jacob* [1950, in *Fetter*, 1994] (see Appendix A).

To solve equation (A3) and (A4) in order to provide estimates of aquifer hydraulic conductivities (Appendix A), the distance x to the tidal body was required. In reality, the distance x changes over time due to the tidal transgression-regression cycle, which is not accounted for in the tidal model used that assumes a vertical tidal boundary. The distance x was then defined using the digital elevation model of the site and four realizations of x; the nearest highest tide level (1.6 m AMSL), the nearest lowest tide level (−1.6 m AMSL), the mean tide level (topographic contour 0 AMSL) and the midtide (midpoint between highest and lowest tides) for each well.

Finally to obtain an estimate of the hydraulic conductivity (K; expressed in m s^{-1}) from the diffusivity values, a local estimate of storativity was required. For a semiconfined aquifer, storativity S was estimated using the water table fluctuation method [*Healy and Cook*, 2002; C. Wilson, Queen's University Belfast, unpublished data, 2011], which in turn was used to estimate transmissivity T and hydraulic conductivity $K = T/b$. In this work, b was assumed as the saturated thickness intersected by the piezometer to reflect the local aquifer volumes affected by the hydraulic tests.

3.5. Groundwater Modeling

3.5.1. Numerical Modeling of Groundwater Flow and Salt Transport

A 3-D variable-density flow and transport model, using the FEFLOW code ver. 6.1 (DHI-WASY) was applied to simulate the coupled flow and salt transport in the aquifer. The numerical model was primarily used to simulate the effect of dykes on groundwater flow and saltwater intrusion and ultimately provide estimates, through model calibration, of the hydrogeological properties of the dykes (primarily hydraulic conductivity, storativity, and effective porosity). The model covered an area much larger than the field study area, including the tidal flat and the mapped geological boundary of the unconfined Sherwood sandstone (Figure 3). The confined sandstone under the overlying Mercia mudstone was not included in the domain but a lateral entering flux was applied from results of previous regional modeling studies [*Dickson et al*., 2014, 2015]. The model contained 236,820 triangular prismatic elements and 129,649 nodes. It was structured in 12 layers, each comprising 19,735 elements, and of thickness exponentially increasing with depth. The elements were designed to match the mapped dyke boundaries and were refined within the dykes. Dykes were computed as vertical features as per results from the forward magnetic modeling (section 4.1.1). The top layer followed the topographic DEM elevation and the bottom layer was fixed at 100 m below sea level to include the whole thickness of the freshwater lens. The hydraulic properties of the host sandstone were fixed from the synthesis of both literature review and the hydraulic tests carried out in this study (section 4.1.3). The

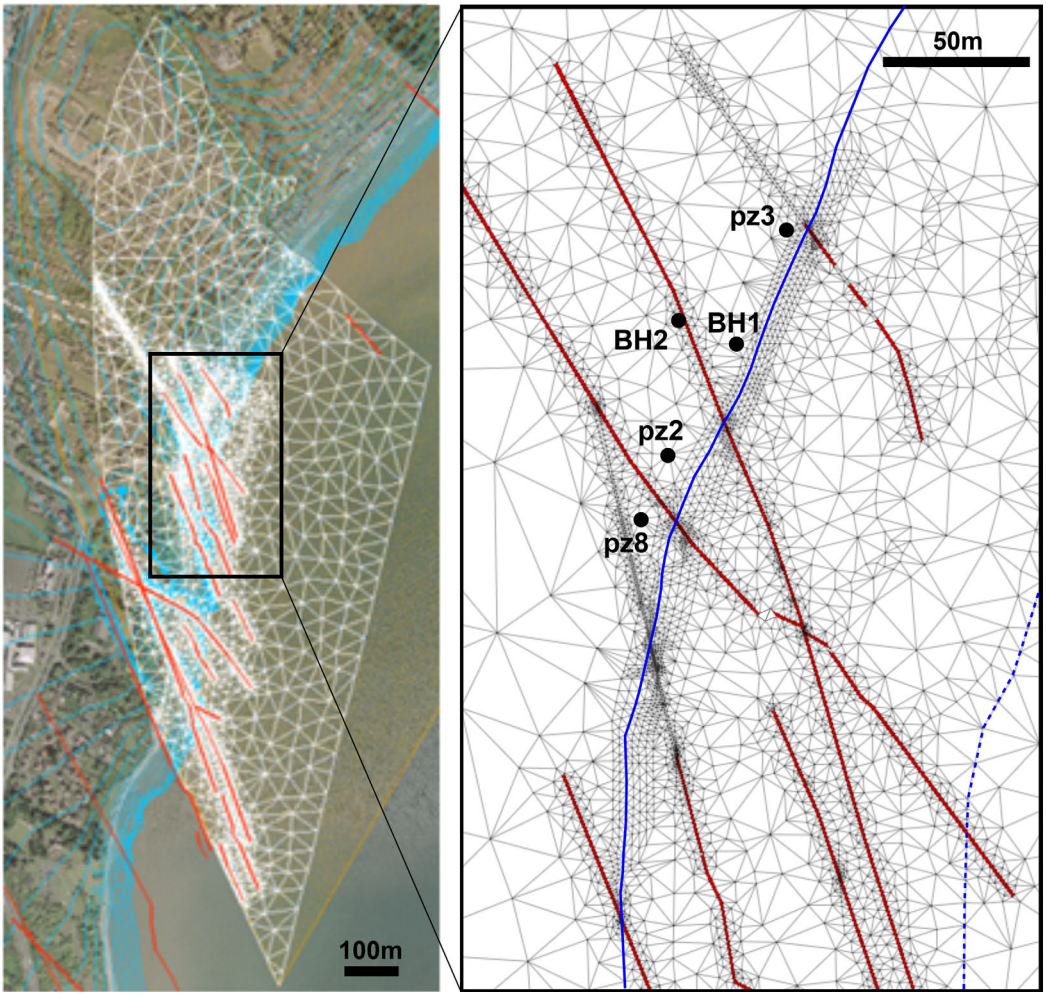

Figure 3. (left) Full model domain with meshing and (right) enlarged field study area. Red lines on left are initial interpretation and extrapolation of dykes extent from aerial imagery. Red lines on right are actual computed dykes from field observations and magnetic data (integrating ground magnetic surveys (Figure 2), airborne magnetic maps (Figure 1), and forward magnetic modeling (section 4.1.1)). On left, light blue contours are the calculated heads from regional modeling [*Dickson et al*., 2015]. On right, plain blue line is the mean high tide level and dashed blue line is the mean low tide level.

hydraulic properties of the dykes were calibrated as part of the modeling (section 4.2). Due to their high-density (dm-scale) of suborthogonal and sublinear fractures, individual dykes in this work were treated as an equivalent porous medium characterized by an equivalent isotropic permeability accounting for both fractures and matrix as established at the studied site by *Dickson et al*. [2014]. Material property values are summarized in Table 2. Groundwater recharge was fixed at 365 mm yr^{-1} from previous regional studies [*Dickson et al*., 2014, 2015]. The sea (Belfast Lough) boundary was applied on the top layer (i.e., the bathymetric surface) of the model using the *VaryingSaltwaterHead* package in FEFLOW and the predicted tidal levels of the Lough [*National Oceanography Centre*, 2011] for the period considered (10 June 2011 to 10 August 2011). The *VaryingSaltwaterHead* package allowed the application of the saltwater tidal fluctuations including the variable tidal extent (adaptive time step of maximum 15 min) that is, the progressive lateral inundation/recession of the tidal flat taking into account the tidal flat topography. A no flow boundary was applied on the vertical offshore face of the model, located at more than 300 m from the mean low tide contour in order to minimize its influence on model results at the site. In the field study area (Figure 3), the topography of the tidal flat was mapped at low tide with a differential GPS at an average resolution of 10 m and incorporated in FEFLOW. On flooded areas, the package was parameterized to apply a varying specified head corresponding to the tide levels and a seawater concentration of 32 kg m^{-3} (or g L^{-1}), which is the average salinity of the Lough. On unflooded area, the package converts the boundary condition as a

Table 2. Groundwater Model Material Properties for Host Sandstone and Dolerite Dykes

Parameter	Symbol	Unit	Value	Source
Sandstone				
Horizontal hydraulic conductivity	K_h	m s^{-1}	1×10^{-7} to 2×10^{-5} increasing with depth	*Robins* [1996] *Yang et al.* [2004] This study (section 4.1.3)
Vertical hydraulic conductivity	K_v	m s^{-1}	$K_h/10$	Calibrated
Specific storage	S_s		1×10^{-4}	Calibrated
Storativity ($=S_s \times b$)	S		1×10^{-2}	Calibrated
Effective porosity	n_e		0.1	Calibrated
Longitudinal dispersivity	α_L	m	1	Calibrated
Transversal dispersivity	α_T	m	0.1	Calibrated
Dolerite Dykes				
Isotropic hydraulic conductivity	K'	m s^{-1}	2×10^{-8}	Calibrated from initial values by *Dickson et al.* [2014]
Specific storage	S_s'		1×10^{-5}	Calibrated
Specific yield ($=S_s' \times b$)	S'		1×10^{-3}	Calibrated
Effective porosity	n_e'		0.01	Calibrated
Longitudinal dispersivity	α_L'	m	0.5	Calibrated
Transversal dispersivity	α_T'	m	0.05	Calibrated

seepage (free draining) face when the simulated heads are higher than the ground elevation or as a recharge face otherwise.

3.5.2. Petrophysical Relationship Between Modeled Pore Water Salinity and Bulk Electrical Resistivity

In order to directly compare the numerical modeling results, i.e., the calculated total dissolved solids (TDS; in kg m^{-3}), with the ERT models, i.e., the bulk resistivity (ρ; in Ω m or m^2 kg s^{-3} A^{-2} in SI units), both data were converted into a common unit. The petrophysical relationship developed by *Waxman and Smits* [1968] extending the model of *Archie* [1942], relating bulk electrical resistivity (ρ) to the pore water resistivity (ρ_w) was utilized (see Appendix B). The relationship developed by Waxman and Smits has the advantage of taking into consideration the clay contribution to bulk resistivity as opposed to that of Archie, which is applicable to sediments without clays only. A summary of the input values used for the Waxman and Smits model (equations (B1)–(B6), Appendix B) are included in Table 3.

3.5.3. 3-D Forward Resistivity Modeling From Modeled Groundwater Salinity Distribution

In order to overcome some of the uncertainties of 2-D resistivity inversion to predict saltwater distribution, i.e., (1) the nonuniqueness of the inversion and (2) the 3-D effect of heterogeneities, the theoretical geoelectrical response (calculated apparent resistivities) of the modeled salinity distribution was directly compared to the apparent resistivities measured on the two transects ERT1 and ERT2. A 3-D extension of the 2-D procedure of *Comte and Banton* [2007] was carried out. The 3-D pore water salinity distribution from the groundwater modeling was converted into bulk resistivity using the Waxman and Smits model described in Appendix B and section 3.5.2. It was assumed that all Waxman and Smits parameters are spatially homogeneous and those of the Sherwood sandstone (Table 3). The petrophysical parameters for dykes are unknown and have therefore been disregarded assuming that due to their small size their influence on resistivity distribution is negligible. Calculated bulk resistivities were interpolated onto a 3-D mesh generated using TetGen [*Si*, 2008], which honored the topography and the electrode locations of the two resistivity profiles. The 3-D mesh was then used as input resistivity mesh in the BERT code [*Rücker et al*., 2006] to calculate the apparent resistivities for the sequences of quadripoles implemented on the electrodes during field

Table 3. Summary of Values Used in Equations (B1)–(B6) for the Sherwood Sandstone Host Rock

Parameter	Symbol	Unit	Source	Value
Formation factor	F^*	Unitless	$F^* = 1/ø^m$	18.1
Excess of surface charge per unit pore volume	Q_v	C m^{-3}	$\rho_g \cdot (1 - ø)/ø \cdot CEC \cdot 96.32 \times 10^6$	3.4
Cementation factor	m	Unitless	*Taylor and Barker* [2006]	1.85
Porosity	$ø$	Unitless	*Robins* [1996]	0.2
Grain density	ρ_g	g cm^{-3}	*Revil et al.* [1998]	2.65
Cation exchange capacity	CEC	meq g^{-1}	*Taylor and Barker* [2006]	0.03372
Max counterion mobility at 25°C	B_0	m^2 s^{-1} V^{-1}	*Revil et al.* [1998]	4.78×10^{-8}
Formation temperature	T_F	°C	Field well logger data	10.5

resistivity surveys. The calculated apparent resistivities therefore account for the 3-D subsurface resistivity distribution and topography. Each apparent resistivity value calculated for each specific quadripole was compared to the measured value for the two alternative hydrogeological models, i.e., with and without dykes. The goodness of fit was quantified through calculation of the R^2 determination coefficient.

4. Results

4.1. Aquifer Structure and Hydraulic Properties

4.1.1. Dyke Delineation From Magnetics and Aerial Imagery

Delineation of the dyke locations within the host rock was provided by both aerial photography interpretation and the magnetic surveys (Figures 1 and 2). The geomagnetic field values for the dykes were relatively high compared to the Sherwood sandstone host rock (~49,800 and ~49,500 nT, respectively). Measurements were carried out along the beach, where the dykes outcrop and were clearly visible on aerial photography, and in the field immediately behind the beach where the dykes were overlain by glacial till. The magnetic ground survey confirmed the presence of crosscutting dykes observable on the tidal flat and revealed their extension inland. Forward 3-D magnetic modeling shows that the dykes are close to vertical and are on average 1–2 m thick (Figure 4).

4.1.2. Saltwater Distribution and Relative Aquifer Compartmentation From Resistivity Tomography

For interpreting the ERT results, it was assumed that the variations in electrical resistivity were predominantly controlled by variations in pore water salinity, since the expected range of resistivity of more or less clayey sand-clay sediments (at constant porosity and pore water salinity) is about 10–500 Ω m, whereas differences in resistivity between salt water and freshwater saturated porous media are typically about 0.1–100 Ω m (3 orders of magnitude) [e.g., *Palacky*, 1988]. In addition, the thicknesses of the dykes (presumably of higher resistivity) were too small (1–2 m) to be clearly picked up by the ERT (2.5 m electrode spacing). The ERT results therefore provided information on subsurface saltwater distribution whose spatial patterns

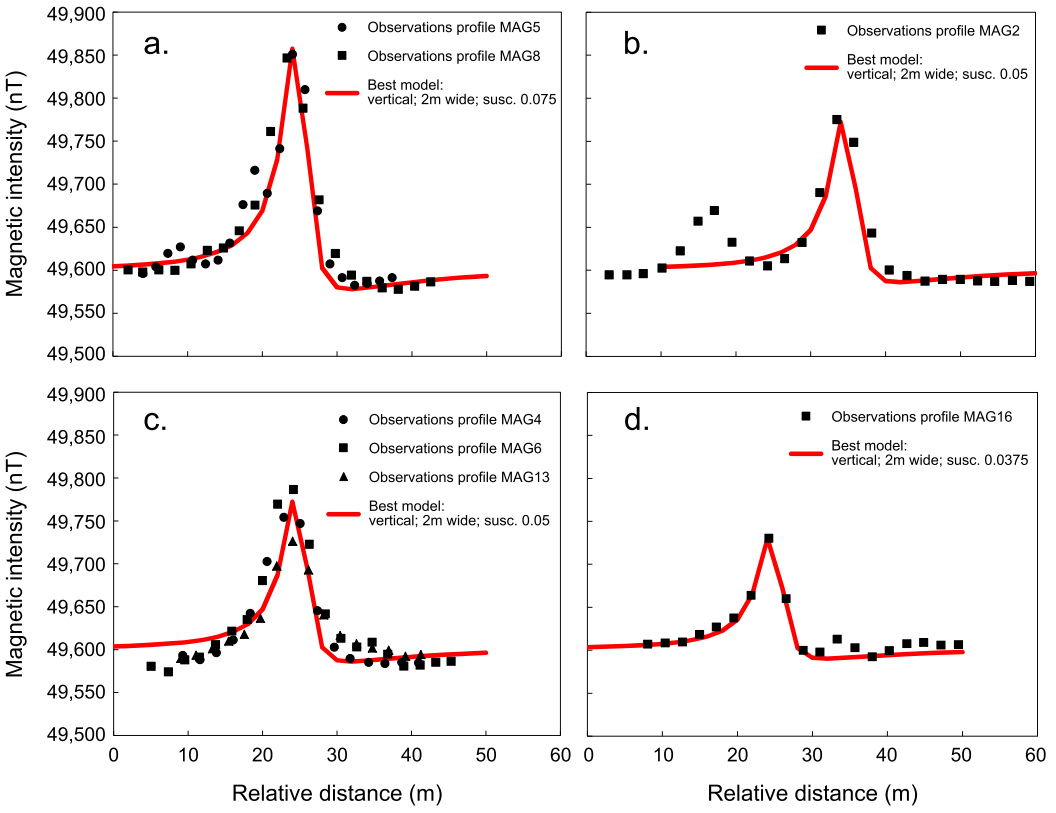

Figure 4. Comparison of observed magnetic field on selected transects with the field computed from forward magnetics modeling (MAG3D code): (a) profiles MAG5 and MAG8; (b) profile MAG2; (c) profiles MAG4, MAG6, and MAG13; and (d) profile MAG16. The best agreements presented here were obtained for vertical dykes, 1–2 m thick. For location of Dykes 1–4, see Figure 2.

revealed a relative aquifer compartmentation with poorly connected groundwater flow units (Figure 5). The relative flow compartmentation can be related to dyke locations as mapped previously. Across the two profiles (ERT1 and ERT2), modeled bulk resistivity values ranged between less than $10^{0.9}$ (=8) Ω m reflecting saltwater-saturated porous medium and $10^{2.1}$ (=126) Ω m reflecting freshwater-saturated porous medium as observed by previous authors in the Sherwood sandstone [e.g., *Taylor and Barker*, 2006]. The lowest (saltwater) resistivities were obtained at shallow depth down to about 5–10 m below the tidal flat (Figures 5a and 5b) and can be interpreted as the saline water recirculation cell due to tides. For ERT1 (Figure 5a), equally low resistivity values were also obtained on the whole depth of investigation below the permanently flooded seafloor, i.e., below the lowest tide level. This would reflect the saltwater wedge dipping landward with a high angle (~80°). Such high angle of the freshwater-saltwater interface is usually observed in low-permeability aquifers [e.g., *Bear et al.*, 1999].

Below land on ERT1, resistivities were also decreasing with depth suggesting possible presence of the saltwater wedge below the ERT model depth (−45 m AMSL). A high resistivity spot was obtained at around −20 m AMSL between the two dykes on ERT1, which may be due to (1) a lateral (3-D) effect where the inverse model produced exaggerated resistivity to account for the two dykes that were simultaneously picked up laterally at about 20 m from the profile and/or (2) lower salinities favored by convergent flow of freshwater between the two dykes. Overall, the distribution of resistivities is consistent with a saltwater wedge dipping landward. The high dipping angle of the wedge and its proximity to the dykes suggest freshwater accumulation upgradient, i.e., that dykes are acting as a relative barrier to flow and saltwater intrusion.

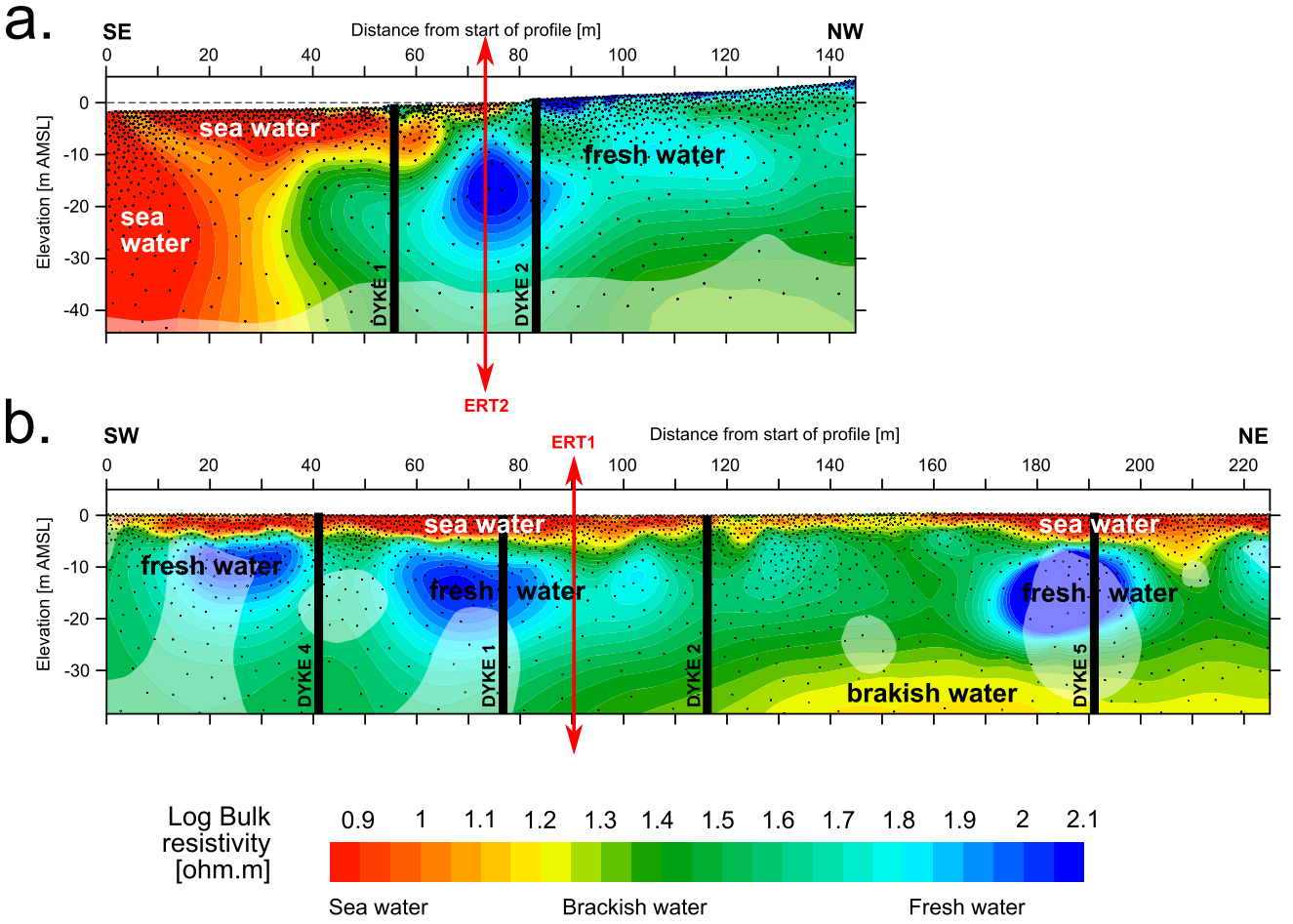

Figure 5. ERT inverted models: (a) ERT1 (1723 elements, 7 iterations, rms = 4.29%) and (b) ERT2 (2680 elements, 5 iterations, rms = 3.57%). Transect locations are indicated in Figure 2. Black points are element centroids. White shaded zones are model areas with DOI > 0.1 [*Oldenburg and Li*, 1999] conventionally indicating model elements that are not well constrained in the inversion. Horizontal axis is distance in meters from start of profile and vertical axis is elevation above mean sea level (Belfast Lough datum). Dyke positions (from outcrop observations, magnetic surveys and aerial imagery) are shown as black vertical lines.

ERT2 was implemented parallel to the shoreline, approximately upon the high tide level. The inverted high (fresh water) resistivities showed important lateral variations suggesting a freshwater lens with varying thickness (Figure 5b). The highest resistivity values, i.e., the less saline groundwater, generally appeared on the SW side of the dykes (specifically Dykes 4, 1, and 5 located at the distances 42, 76, and 191 m along the profile, respectively). Similarly to ERT1, this would suggest an accumulation by convergent flow of fresh water on the side of dykes facing groundwater flowing from the land (Figure 2). This again is consistent with a relatively low permeability for the dykes. As a result salt and brackish water would be expected at deeper depth in these locations, which is consistent with the brackish water that was imaged at shallower depths (∼−30 m AMSL) in the areas where dyke density was lower (higher distance of separation) and dykes were less continuous, such as NE of Dyke 2 (Figures 2 and 5b).

In summary, the distribution of freshwater and saltwater is indirectly suggestive of dykes of permeability lower than the relatively homogeneous host sandstone. This results in relative compartmentation of groundwater flow units with water table elevation and saltwater depth controlled by both the amount of groundwater that is captured from upgradient and a partial hydraulic connectivity with surrounding dyke-bounded sandstone units.

4.1.3. Aquifer Hydraulic Properties

The results of hydraulic testing (pump and slug testing) of the wells along with the estimates of hydraulic conductivity from tidal attenuation analysis are summarized in Figure 6.

A large variability of results can be seen between each of the methods used (up to 5 orders of magnitude) with calculated hydraulic conductivities K ranging 3×10^{-8} to 4×10^{-3} m s^{-1}. Hydraulic tests consistently yielded the lowest K values, in the order of 10^{-7} m s^{-1} (Figure 6a). The lowest value was obtained for BH2 that is suspected to be drilled within Dyke 2 metamorphic contact zone (baked zone). Using those K values and the values of pumping rate and duration for BH1 and BH2, it was possible to roughly estimate the maximum radius of influence of the pumping tests. The local storativity value of 1×10^{-2} estimated from the water table fluctuation method was used and assumed to reflect the semiconfined conditions observed at both regional and local scale (at the study site the piezometric level was fluctuating above and below the base of the confining clay till). The simple *Cooper and Jacob* [1946] solution gave a radius of influence of the drawdown cone of 5.5 m for BH1 and 2.2 m for BH2. Another estimate was provided by assuming that groundwater was released from lateral drainage equally distributed along the whole saturated thickness of the wells. In this case, a simple volume calculation gave an average radius of drainage of 0.7 m for BH1 and 0.2 m for BH2. This implies that the hydraulic parameters obtained were representative of the near-well aquifer, i.e., very local, and may have been affected by near-well clogging during drilling (auger).

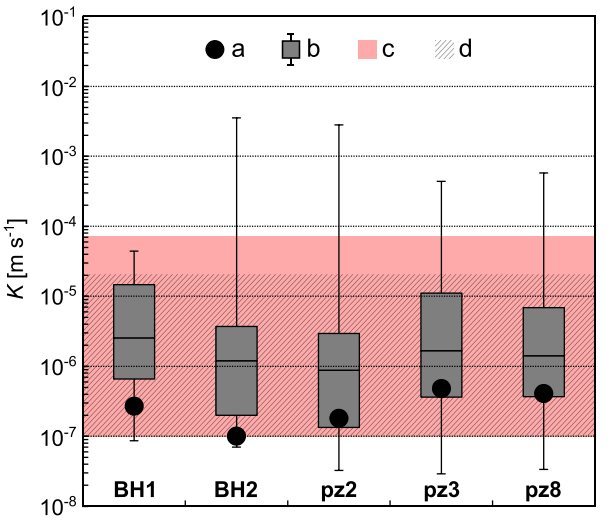

Figure 6. Summary of Sherwood sandstone hydraulic conductivity estimates from (a) hydraulic testing (pump and slug tests) and (b) tidal attenuation analysis (combined tidal efficiency and tidal lag); equations (A3) and (A4) with comparison to ranges of (c) published values at the regional scale and (d) calibrated values used in the groundwater model (Table 2).

The tidal analytical solution provided high ranges of values 3×10^{-8} to 4×10^{-3} m s^{-1} (Figure 6b), which reflects the variability in the choice of the distance x in equations (A3) and (A4) (mean high tide, mean tide, midtide, or mean low tide). However, 50% of the values fell between 1×10^{-7} and 2×10^{-5} m s^{-1}, i.e., across 2 orders of magnitude and in average 1 order of magnitude higher than the hydraulic test values. The hydraulic tests provided more local hydraulic properties, i.e., values that represent the top of the Sherwood sandstone in which the wells were drilled, which in this area is a transitional facies toward the overlying Mercia mudstone. This implies a more clayey lithology which resulted in lower K (and slightly lower electrical resistivities). The tidal attenuation method is more integrative spatially and therefore influenced by both the

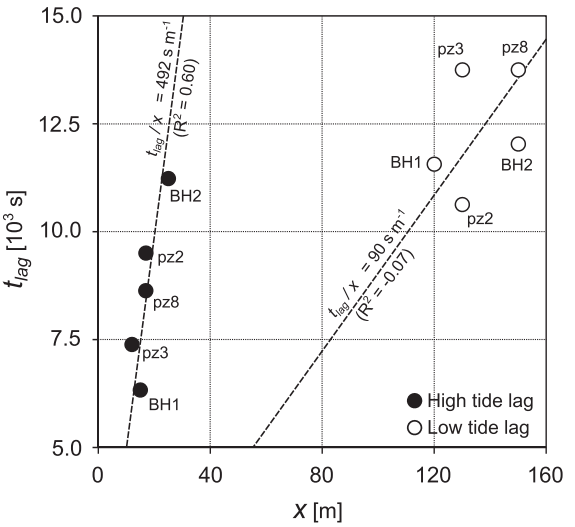

Figure 7. Average time lag of response t_{lag} of the wells to high and low tides versus their distance x to the tidal boundary (mean high tide and mean low tide, respectively). Dashed lines are the best Jacob's analytical solutions (equation (A2)) with coefficients of determination R^2 showing good fit at high tide but poor fit at low tide.

underlying coarser (higher *K*) sands and the lower *K* dykes when located between the tidal boundary and the observation well (BH2 and pz2). The majority of values obtained are within the lower to middle range of reported regional values for the Sherwood sandstone (Figure 6c). The overall lowest *K* values obtained for BH2 and pz2 are reflecting an apparent decrease in *K* due to enhanced tidal attenuation as a result of the presence of Dykes 1 and 2.

The specific analysis of the time lag in the well response to tides (equation (A2)) yielded additional insights in the hydrodynamic attenuation caused by the dykes. At high tide, all well lags were linearly correlated ($R^2 = 0.60$) with the wells' distance to the high tide, as predicted by Jacob's analytical solution (Figure 7). At low tide however, the correlation to low tide distances was poor ($R^2 = -0.07$). This suggests that all wells are hydrodynamically poorly connected to sea level at low tides, because of the presence of dykes. At high tide however, when sea level overflows the dykes they become well connected to the sea through a relatively homogeneous porous media; in this case the attenuation of the tidal signal is therefore only a function of the distance to the sea.

Overall, notwithstanding errors resulting from the assumptions in both hydraulic tests and Jacob's solutions, the majority of *K* values obtained compare well with the ranges provided by previous authors for the upper layers of the Sherwood sandstone at the regional scale; i.e., 1.0×10^{-7} to 6.6×10^{-5} as reported by *Robins* [1996] from pumping test data, and 3.5×10^{-7} to 5.2×10^{-5} m s^{-1} by *Yang et al.* [2004] from regional numerical modeling. They also clearly reveal the influence of the volcanic dykes that express hydrodynamically as an apparent decrease in aquifer hydraulic conductivity and an apparent increase of the distance to the sea.

4.2. Quantitative Analysis of the Impact of Dykes on Groundwater Flow and Saltwater Intrusion

4.2.1. Groundwater Heads Monitoring and Modeling

Figure 8 shows the recorded groundwater time-series at the site for the period 10 June to 10 August 2011 including daily rainfall, along with a 7 day snapshot (28 June to 5 July 2011) of the time series data with no rainfall. Both also include the local predicted tide [*National Oceanography Centre*, 2011].

A high variability in the response of the aquifer to the tidal signal was clear at the different piezometer locations, considering that wells BH1, pz2, pz3, and pz8 are all approximately equidistant from the shore. All wells reacted consistently and rapidly to periods of intense recharge, which was most clear between the 21–26 July during a period of heavy rainfall. BH1 and pz3 responded almost identically to both the semidiurnal tidal component and the spring-neap (twice monthly) tidal component, showed very little signal attenuation and had the lowest water table elevation. These zones are not separated from the sea by continuous dykes (Figure 2). Well pz2 which is located in a closed dyke-bounded block is relatively isolated from the sea and showed almost no discernible response to the semidiurnal tide (high frequency) component but still showed evidence of a spring-neap (lower frequency) response, and had the highest water table elevation. Well pz8 which is only partially isolated from the sea showed an intermediate water table elevation and a visible response to the semidiurnal tide although highly attenuated.

While the models were run for the entire observation period, Figure 9 compares the water level observations with the results of the numerical models for the selected 7 day period without rainfall, in order to avoid comparison with observed fluctuations containing both the tidal signal and the recharge signal. Two numerical models were considered; one with low permeability and storativity values of about 100 times

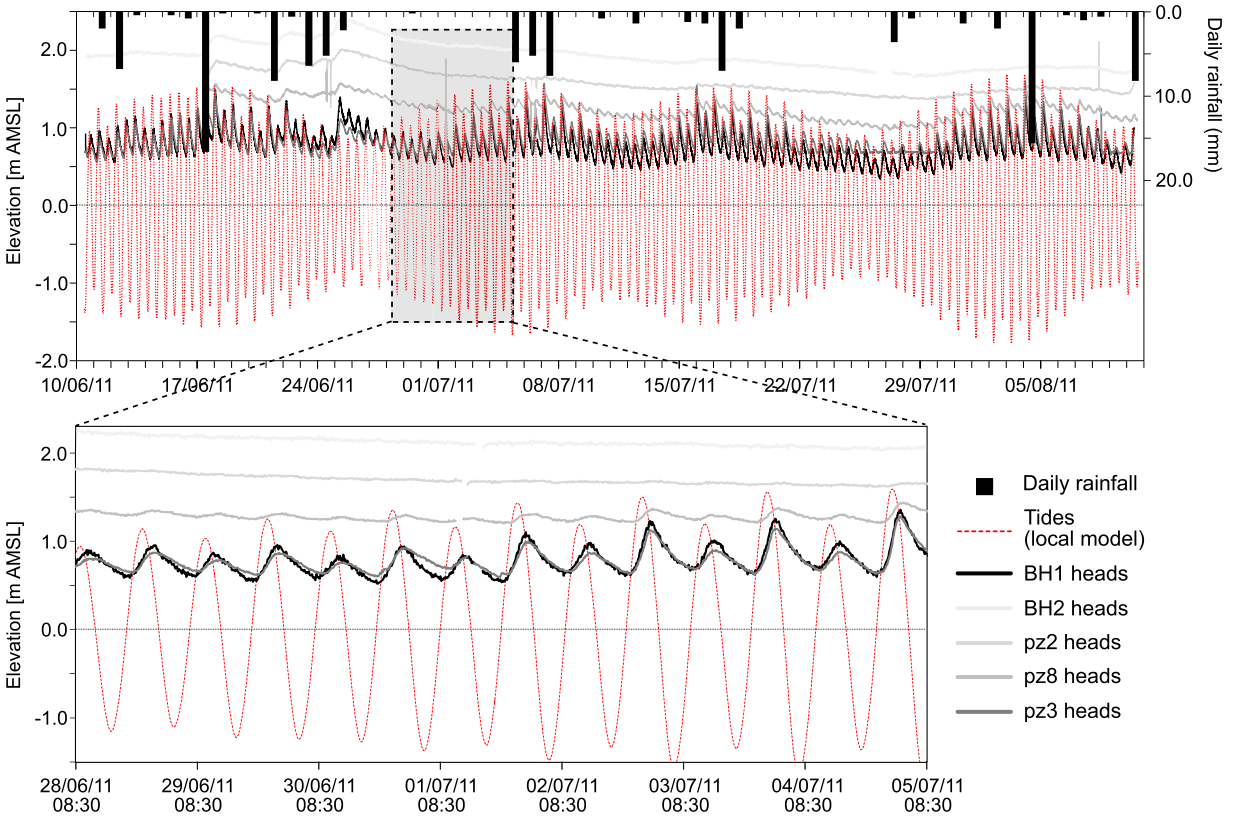

Figure 8. Groundwater monitoring results for wells at the site. Levels are referenced to AMSL (above mean sea level, Belfast Lough datum). Total daily rainfall was measured at QUB GAP weather station (QUB GAP, 2014) and the modeled tide of Belfast Lough was derived using POLTIPS-3 software [*National Oceanography Centre*, 2011].

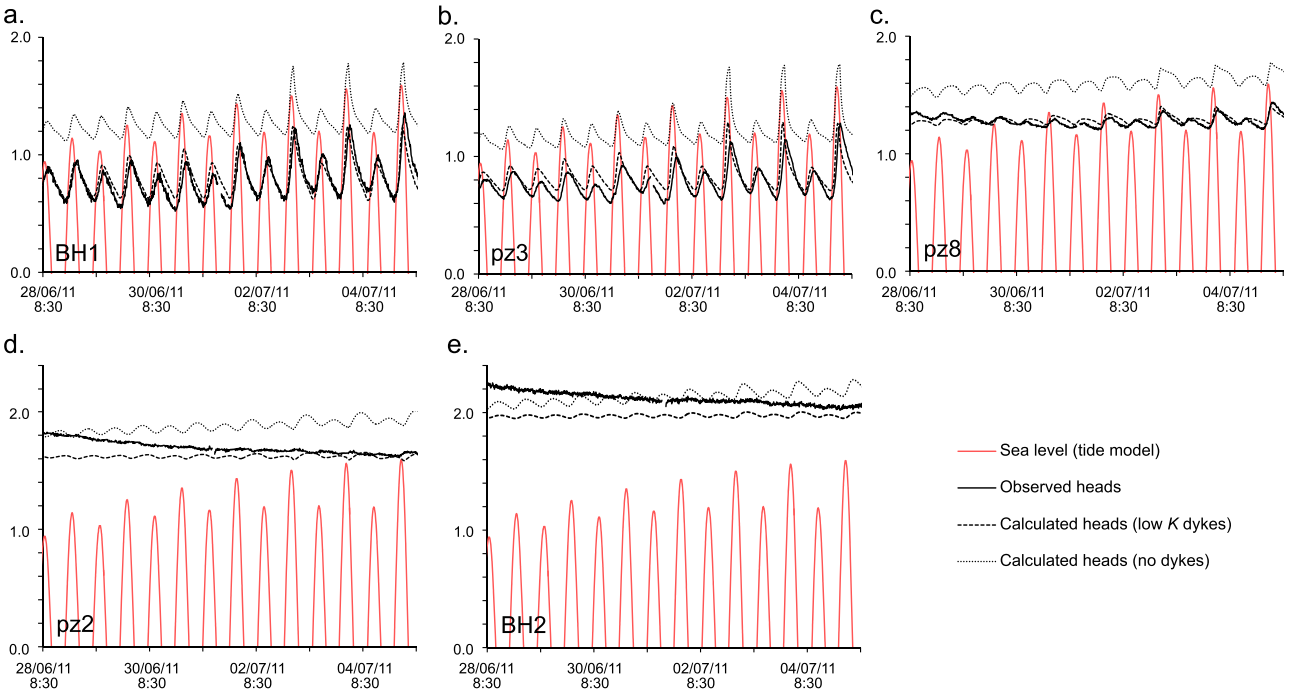

Figure 9. Comparison of observed versus calculated heads for the 7 day period 28 June to 7 July 2011 without rainfall (enlarged in Figure 8), for wells (a) BH1, (b) pz3, (c) pz8, (d) pz2, and (e) BH2. Calculated heads were extracted from two different conceptual models (1) a model computing low-permeability/storage dykes (Table 2) plotted as a dashed black line and (2) a model without dykes plotted as a dotted black line. In the model without dykes, the hydraulic properties at the dyke locations were replaced by the local properties of the host sandstone.

and 10 times lower than those of the host sandstone, respectively (see Table 2); and one with no dykes, i.e., with the same properties as the host sandstone. Figure 11 also shows midtide spatial distribution of simulated groundwater heads at three different depths (the water table depth, −20 m AMSL and −50 m AMSL).

Calculated heads in the presence of dykes showed a very good match with the observations for BH1, pz3, and pz8 (Figures 9a–9c), while a reduced but still reasonable comparison existed for pz2 and BH2 located within the closed sandstone unit between Dykes 1 and 2 (Figures 9d and 9e). Calculated head amplitudes for pz2 and BH2 were close, although slightly higher, to the observations; however, a lag of about 6 h resulted in out-of-phase fluctuations. Also, the effect of the previous recharge event seen as a slow decay of observed heads was not reflected in the calculated heads. This may be due to locally lower storativity in the vicinity of pz2 not accounted for in the model, or some clogging in the piezometer sand pack. In contrast, calculated heads in the absence of dykes clearly differed from the observations, both in absolute elevation and in amplitude. Simulated heads were on average between 20 and 40 cm higher. This suggests a higher groundwater inflow from the recharge area inland that is not in this case diverted in the southern direction by the relative barrier effect of the dykes, as located in Figure 2. In the presence of dykes (in average oriented NNW-SSE), part of the groundwater originating from the upland recharge area does not flow along the SE-oriented shortest path toward the shore but tends to flow parallel to the dyke network in the southern direction, resulting in lower water tables at the monitored site. In addition, in the absence of dykes, the head amplitudes particularly for the wells located upgradient of the dykes (BH2, pz2, and pz8) appeared much higher than the observations (Figures 9c–9e), which would confirm the attenuation role of the lower permeability/storativity dykes.

Figure 10 provides a comparison between the Jacob analytical solution (equation (A1)) and both the experimental data and model results for the ranges of observed tidal H_0 and piezometric H_x amplitudes, and for fixed values of x on one hand (taken as the geometric mean between high and low tide) and K on another hand (geometric mean). The experimental data showed a clear nonlinear relationship between H_0 and H_x which contradicts the linear solution of Jacob. The nonlinear H_x response was reflected by higher piezometric amplitudes at high tide which resulted in (1) apparent higher K values or (2) apparent lower tidal distance x. This was a result of the moving tidal boundary on the actual topography of the tidal flat whereas the Jacob model assumes a fixed, vertical tidal boundary at distance x. The nonlinear effect of the complex tidal boundary was confirmed by the results of the 3-D numerical models that are also plotted for comparison. Both numerical models (with and without dykes) honored the observed nonlinearity, however, the model that did not account for low-permeability dykes showed a clear deviation from the experimental data particularly for wells located behind continuous dykes (BH2 and pz2).

Overall, the joint analysis of calculated and observed groundwater heads indicates the role of the dykes in partial compartmentation of groundwater flow units at the site scale. Both clearly show the attenuation of the semidiurnal tidal signal at the observation points pz2 and pz8 as a result of the dyke hydrodynamic properties and orientation with respect to the well positions. However, the dykes had a reduced effect on the twice monthly spring-neap tidal cycle whose response was observed in all the wells (Figure 8). This is of importance in terms of groundwater resource management. As observed in many technical groundwater studies, dykes would affect borehole efficiency (higher drawdowns in dyke-bounded aquifer blocks) when subject to high abstraction rates on short durations. This would be less significant over longer durations in terms of groundwater equilibrium for example or when pumping regimes are constant over long periods with lower abstraction rates.

4.2.2. Saltwater Transport Modeling and Calibration to Geophysical Inversions

The transport of salt in groundwater was fully coupled with the flow in the variable-density modeling code and the calculated saltwater distribution for an average midtide configuration is presented in Figure 11, along with the calculated groundwater heads. Due to the shallow depths of the monitoring wells, the groundwater electrical conductivity recorded together with the heads only showed tide-induced variations that were within the logger accuracy range, i.e., 1 μS/cm. Therefore, the observations of groundwater salinity in wells did not provide insights on the dynamics of salt transport. The groundwater salinities coinciding with the ERT profiles were extracted from the groundwater model for comparison with the cross-sectional distribution of resistivity provided by the ERT (Figure 12). The correlation between the bulk electrical resistivities provided by ERT and the modeled pore water salinity was established using the petrophysical model detailed in section 3.5.2 and both cross sections with a common color scale are plotted in Figure 12.

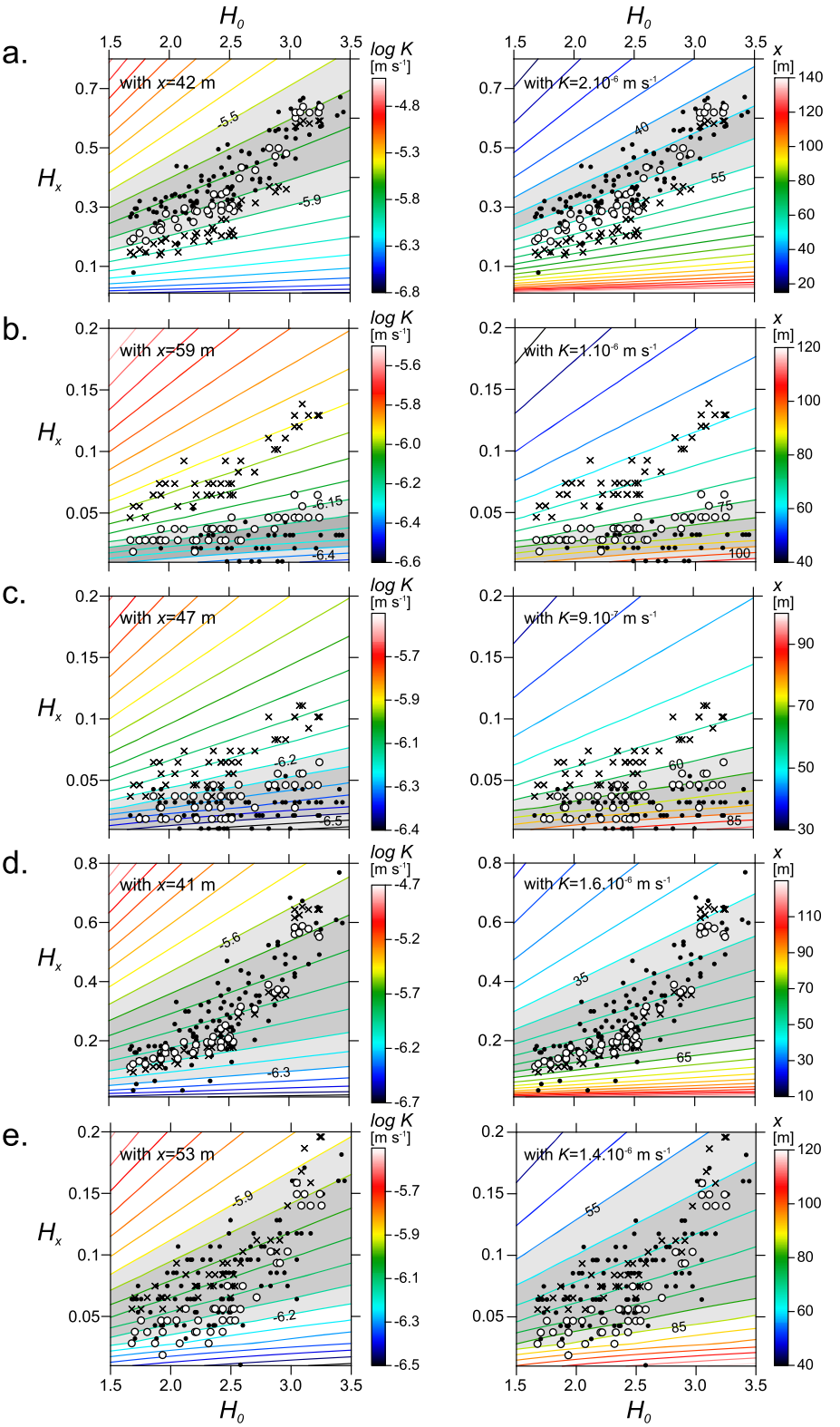

Figure 10. Theoretical solutions of Jacob's analytical model (gradual color lines) for the observed ranges of tidal and piezometric fluctuations overlain by the experimental data (black points) and the results of the 3-D numerical models (white-filled circle symbols for the model with dykes; cross symbols for the model without dykes) for the five observation wells: (a) BH1, (b), BH2, (c) pz2, (d) pz3, and (e) pz8. (left) *K* solutions assuming a constant *x* taken as the geometric mean of the distance between mean high and mean low tides; (right) the *x* solutions assuming a constant *K* taken as the geometric mean of *K* values from the analytical ranges shown in Figure 6.

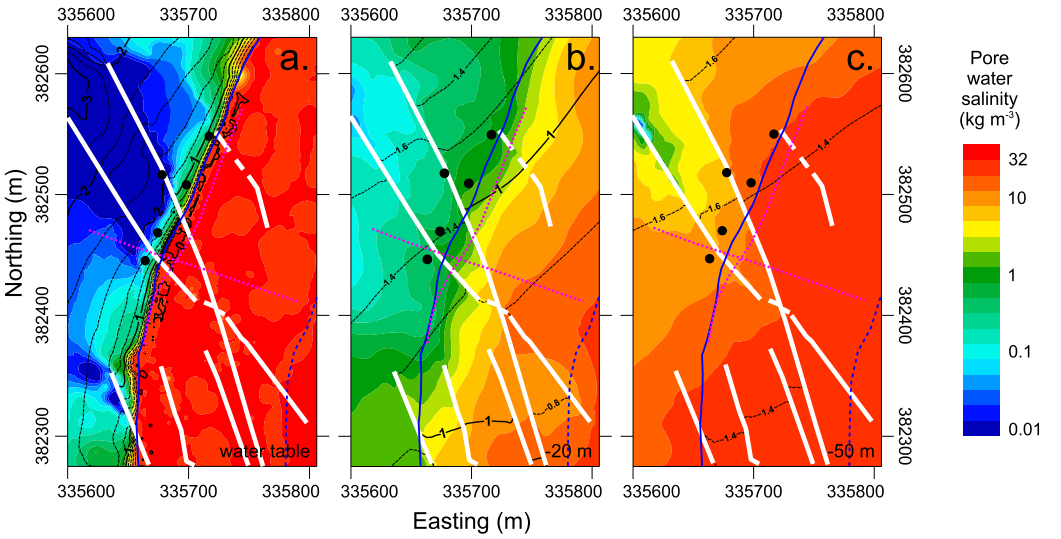

Figure 11. Modeled spatial distribution of groundwater heads (plain and dashed black lines, in m AMSL) and salinities (color scale, in kg m^{-3}) for an average midtide at three different depths, (a) the water table depth, (b) −20 m AMSL, and (c) −50 m AMSL. Black dots are well locations; white lines are dyke locations; plain blue line is the mean high tide level and dashed blue line the mean low tide; dotted white lines are the locations of the ERT profiles.

Calculated salinity maps at different depths (Figure 11) show complex patterns of saltwater distribution in relation to dyke occurrence. At shallow depth, i.e., at the depth of the water table (Figure 11a), the aquifer below the mean high tide level, including dykes and host sandstone was fully saturated with saltwater close to the sea concentration (32 kg m^{-3} locally). Above the mean high tide level the aquifer was saturated with fresh water at concentration lower than 1 kg m^{-3}. The lowest salinities (∼0.01 kg m^{-3}) occurred in the vicinity of the sandstone unit bounded by Dykes 1 and 2 that intersect on the tidal flat, which also displayed the highest groundwater heads of mostly above 2 m AMSL. There was a sharp transition between fresh and salt water at the mean high tide line. This distribution in the shallow surface has been clearly confirmed by the inverse resistivity models of Figure 12. At a depth of −20 AMSL, the transition zone between fresh and salt water was calculated as much wider (>200 m), which can be partially explained by a coarse vertical mesh resulting in higher numerical dispersion (Figure 11b). However, spatial salinity patterns influenced by dyke occurrence were also clearly visible. Upgradient, the freshest groundwater was mostly restricted to the western side of Dykes 1 and 2 that favored enhanced fresh water inflows from the recharge areas. Groundwater heads were also higher on that side of the dykes. More so below the tidal flat, dykes were responsible for sharp steps in the distribution of heads and salinities and local freshwater inflows on the western side of dykes. This was in good agreement with the two resistivity profiles of Figure 12, and especially the profile ERT2 parallel to the shoreline (Figure 12b). At a depth of −50 m AMSL, the aquifer was almost entirely saturated with saltwater (Figure 11), except in the "closed" aquifer unit bounded by Dykes 1 and 2 where brackish water was still present up gradient. That depth likely corresponds to the approximate base of the freshwater lens as suggested by the resistivity models (Figure 12).

The modeled salinities were overall in relatively good agreement with the corresponding resistivity cross sections. The comparison plotted in Figure 12, using a direct relationship between pore water salinity and bulk resistivity shows that both models consistently produced the same patterns of seawater intrusion, including (1) high salinities at shallow depths below the tidal flat corresponding to the tidal saltwater recirculation cells; (2) lateral variations of the freshwater thickness between dyke-bounded sandstone units, particularly below the tidal flat; and (3) enhanced fresh water inflows on the side of the dykes facing inland aquifer recharge areas. More specifically, the thickness variation of freshwater lenses was in good agreement between the groundwater and resistivity models. Regarding the overlying shallow recirculation cells, although their average thickness was consistent in both models, their lateral variation showed differences. This may be due to local effects of the topography and/or sea hydrodynamics, such as waves or occurrence of temporary seawater puddles at low tide (as observed in the sandstone unit bounded by intersecting Dykes 1 and 2) that were not accounted for in the groundwater models. Finally, the resolution of both

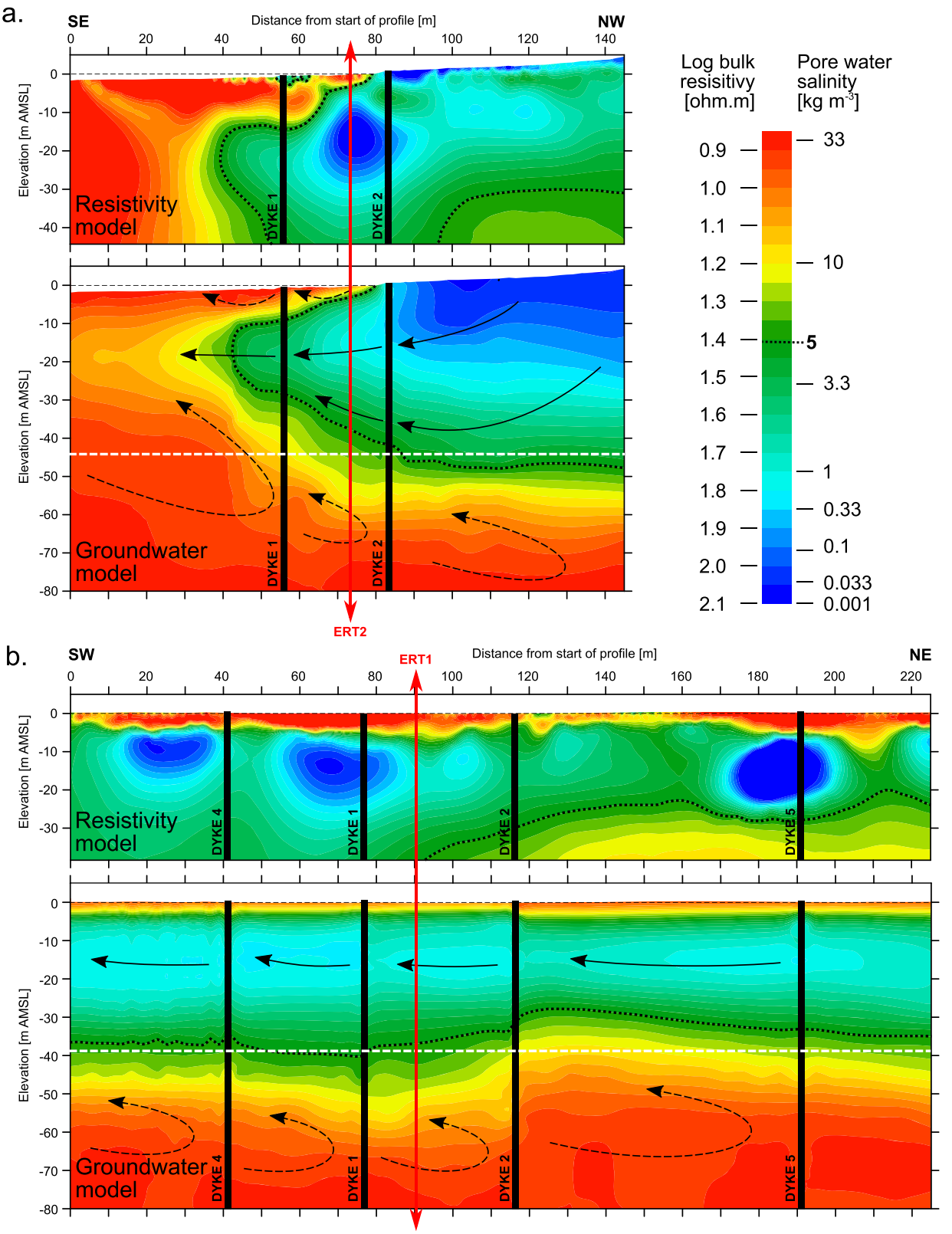

Figure 12. Comparison of inverse ERT models and 3-D groundwater model results using common dual-entry bulk resistivity/pore water salinity color scale obtained from the application of the *Waxman and Smits* [1968] petrophysical model; (a) cross section perpendicular to the shore coinciding with ERT1 and (b) cross section parallel to the shore coinciding with ERT2. The same spatial scale as for Figure 5 is used. Black vertical lines are dyke locations and vertical red arrows mark the intersection of the two cross sections. Black arrow on the groundwater model sections are simplified groundwater flow paths (projected and unscaled); plain arrows for freshwater, dashed arrows for saltwater. The white dashed lines indicate the maximum depth imaged by the ERT profiles.

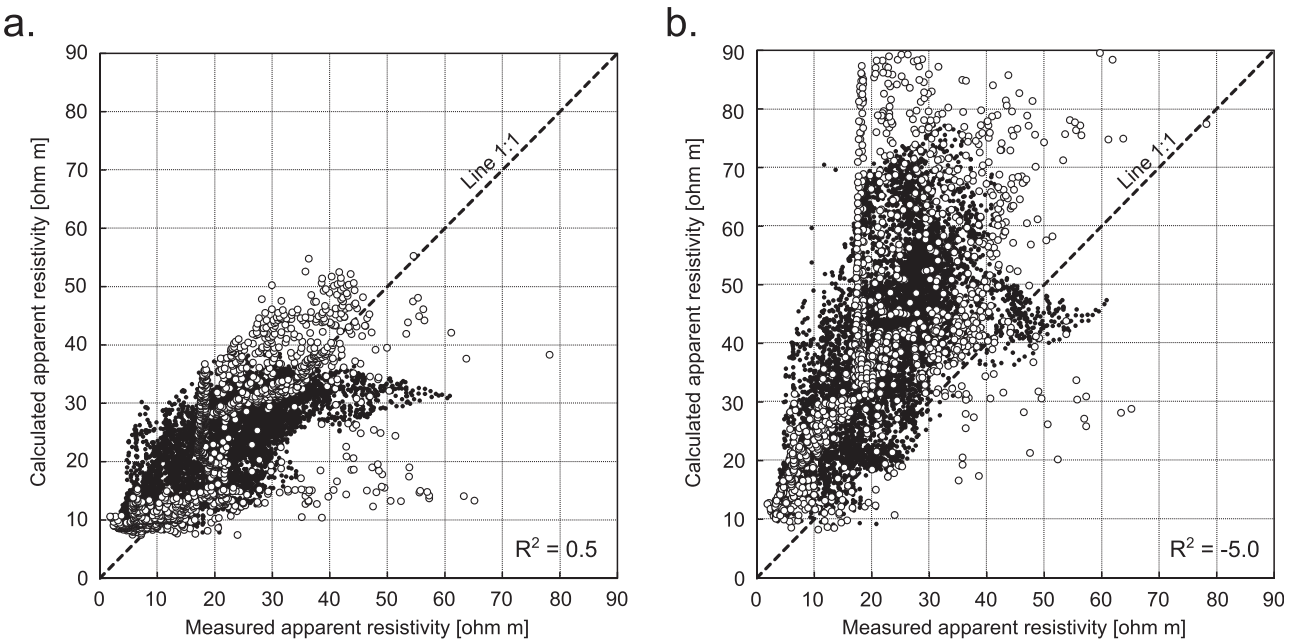

Figure 13. Comparison of the measured apparent resistivities from ERT surveys with the apparent resistivities calculated from the groundwater model (a) with dykes and (b) without dykes. White-filled circles are ERT1 data; black dots are ERT2 data.

models over the cross sections also differed; the 2-D resistivity models (~0.3 model elements per m^2) having in average 10 times higher resolution than the 2-D sections extracted from the 3-D groundwater model (~0.03 model node per m^2). This resulted in shaper contrasts/more blocky distribution of resistivity and smoother variations in salinity, respectively.

4.2.3. 3-D Forward Resistivity Modeling Verification

Due to nonuniqueness in resistivity inversion and, importantly, to the lateral influence of 3-D heterogeneity on the observed apparent resistivities, the 2-D inverse models are expected to contain inaccuracies and distortions. To overcome these issues, the forward apparent resistivities calculated with BERT from the 3-D saltwater distribution simulated by the groundwater model were compared to the measured apparent resistivities (Figure 13), which provided a more direct quantitative assessment of the groundwater model results [*Comte and Banton*, 2007]. Comparison shows that there is a relatively good agreement between calculated and measured resistivities when the low-permeability dykes were included in the groundwater model ($R^2 = 0.5$), whereas a very poor correlation is observed when the dykes were not accounted for ($R^2 = -5.0$). For both models, the spread of data points may be attributed to the simplification of dykes and sandstone properties as spatially homogeneous, which resulted in oversmoothing salinity and therefore resistivity distribution. In contrast, resistivity imaging, in addition to being able to pick small scale subsurface heterogeneities, was also subject to noise related to the variable quality of electrode contacts (relatively contrasted in the tidal zone due to alternating conductive saltwater and dry sands on short length scales) increasing the variability in measured data. In addition, the unsaturated zone characterized by an increase in resistivity due to variable pore saturation has not been accounted for in the forward 3-D resistivity modeling, which explains that the highest observed resistivity values (>50 Ω m) were not well matched by the calculated resistivity values. The groundwater model without dykes generally showed much higher calculated apparent resistivity related to a freshwater lens that was thicker and more extended offshore. This was the result of a higher freshwater inflow from inland recharge, which otherwise was limited by the presence of Dykes 1 and 2 that tend to direct groundwater flow southward (Figure 13). This was consistent with the general higher average water table simulated in the absence of dykes (Figure 9). The forward resistivity modeling therefore further confirms the significant impact of the dykes on the groundwater flow field and salt water intrusion.

4.3. Summary of Calibrated Parameters and Contrasts of Properties

As for most volcanic settings—and more widely most hydrogeological settings with complex distribution of small heterogeneities—the properties of the volcanic dykes in the studied region were largely unknown on

Table 4. Final Estimated Hydrogeological Properties for the Dykes and Comparison With the Host Sandstone

Parameter	Volcanic Dykes	Host Sandstone (Local:Whiteabbey)	Host Sandstone (Regional[a]:Lagan Valley)	Ratio Sandstone/ Dyke (Local)	Ratio Sandstone/Dyke (Regional)
Horizontal hydraulic conductivity K_h (m s^{-1})	2×10^{-8}	1×10^{-7} to 2×10^{-5}	1×10^{-7} to 7×10^{-5}	5–1000	5–3500
Specific storage Ss (m^{-1})	1×10^{-5}	1×10^{-4}	1 to 2×10^{-4}	10	10–20
Storativity S	1×10^{-3}	1×10^{-2} [b]	$\sim 2 \times 10^{-3}$	10	2
Effective porosity n_e	1×10^{-2}	1×10^{-1}	1 to 3×10^{-1}	10	10–30

[a]From *Bennett* [1976], *Robins* [1996], *Kalin and Roberts* [1997], *McNeill et al.* [2000], *McKinley et al.* [2001], *Yang et al.* [2004], *Cronin et al.* [2005], and *Dickson et al.* [2015].
[b]Based on model thickness of 100 m.

the field and this, despite multiple studies acknowledging their role as relative barriers to groundwater flow [*Bennett*, 1976; *Robins*, 1996; *Kalin and Roberts*, 1997; *Cronin et al*., 2005]. Using multiple constraints (high frequency groundwater monitoring data, high resolution magnetic and geoelectrical data), the calibration of the groundwater models using a trial-and-error procedure has provided quantitative estimates of the dykes hydrogeological properties, i.e., values of hydraulic conductivity K (isotropic), specific storage Ss, storativity S, and effective porosity n_e of 2×10^{-8} m s^{-1}, 1×10^{-5} m^{-1}, 1×10^{-3}, and 1×10^{-2}, respectively (Tables 2 and 4). The parameter sensitivities along with the next challenges in improved parameterization are discussed in section 5. These values indicate large contrasts of properties with both the local and regional values for the host sandstone (Table 4), which result in major alterations of groundwater pathways at the field scale as shown in the previous section.

5. Discussion

The multiphysical investigations and modeling approach that are presented have provided multiple constraints on the conditions of groundwater flow and salt transport in the complex studied aquifer. While the field-scale hydraulic properties of the host sandstone can be directly and relatively easily obtained from traditional hydrogeological investigations such as hydraulic tests, the field-scale hydraulic properties of volcanic dykes cannot, due to their discrete nature, small size, and complex geometry. Combining tidal attenuation analysis with magnetics, resistivity, and variable-density flow modeling enabled constraint of the intrinsic properties of the dyke and quantification of their impact on the dynamics of groundwater flow and saltwater transport.

First, the magnetic investigations together with outcrop mapping from aerial imagery have provided dyke location both on the tidal flat and on land. Forward magnetics modeling has provided dipping angle of the dykes. Resistivity imaging with ERT has revealed complex patterns of fresh water/salt water distribution in the aquifer that can be related to a relative aquifer compartmentation caused by the dyke intrusions. Well installation and subsequent hydraulic tests have provided local hydraulic properties values for the host sandstone. Groundwater monitoring and tidal attenuation analysis have provided additional, more spatially integrative, values of hydraulic properties. They have also provided evidence of the heterogeneity in these properties introduced by the presence of the dykes and temporal variations in groundwater-seawater connection during tidal cycles. Finally, the groundwater numerical modeling constrained by the multiphysical investigation data has enabled (1) the simulation of the complex 3-D spatiotemporal distribution of heads and salt in the aquifer, revealing the role of barrier to groundwater flow of the dykes that focus freshwater inflow along their boundaries facing the recharge area inland; (2) the estimation of the intrinsic hydrogeological properties of the dykes.

The magnetic surveys have been particularly useful to (1) map the dyke locations inland where no outcrop is present and (2) estimate through forward modeling the dykes dipping angle, which revealed to be steep to vertical (90°). However, the comparison of magnetic maps with the outcropping dykes on the tidal flat has also revealed discrepancies. Locally on the tidal flat, magnetic anomalies have been attributed to the accumulation of volcanic boulders in depression from the erosion and transport of dyke fragments by the sea. Those local anomalies were not accounted for in dyke mapping and groundwater modeling. Also, some dykes that were observed visually both on the field and on the aerial photography (e.g., Dyke 5; Figure 2) did not produce clear magnetic anomalies, perhaps because of originating from a different phase of

volcanism characterized by lavas with low magnetic susceptibility. This implies that on the land, where no outcrop is available, additional (low susceptibility) dykes may be present. In the groundwater modeling, we assumed all dykes extending perfectly vertical and continuous. A more detailed computation of dykes occurrence, continuity, and angle would require further magnetics investigations and 3-D magnetics modeling at higher resolutions, and the use of vertically unstructured meshes for the groundwater model.

Regarding the well testing and groundwater monitoring, some limitations can be pointed out. The observation wells were drilled at relatively shallow depths ($<$5 m) as compared to the depth of the base of the aquifer in the area, which was assumed from regional knowledge [e.g., *Dickson et al*., 2015] to be at around 200 m below sea level. Because of the low spatial influence of the short duration pumping and recovery tests as well as the slug tests, the hydraulic properties obtained are likely to be representative of a limited volume of aquifer around the wells. The relatively low values of hydraulic conductivity obtained (more than 1 order of magnitude lower than the published regional value of the Sherwood sandstone) [e.g., *Dickson*, 2014, 2015] have been explained by the wells being completed within the upper part of the sandstone, which corresponds to a more clayey transitional facies with the overlying Mercia Mudstone [*Robins*, 1996; *Mitchell*, 2004]. In contrast, the higher values obtained from tidal attenuation analysis were about 1 order of magnitude higher, which is closer to the regional *K*. Because the tidal attenuation involves pressure transfers that affect larger aquifer volume, this suggests that *K* is increasing with depth toward values close to the well-established regional *K*. This conceptual interpretation was applied to the numerical model; however, the modality of the vertical variations of *K* at the site is not well known and would require deeper boreholes. Such deeper boreholes would also allow for higher values and variations of groundwater electrical resistivity to be monitored and included in the model calibration for salt transport. Also, despite high temporal resolution of the groundwater monitoring (10 min) the total monitored period was of only two months, which does not allow for capturing possible seasonality in the groundwater response. However, the close proximity of the wells to the shore implying a strong hydrodynamic control by the tides (Figure 8), along with the relatively low rainfall seasonality in Northern Ireland (UK Met Office data available at http://www.metoffice.gov.uk/climate/uk/regional-climates/ni) would both suggest that the monitoring period provides a reasonable calibration data set for the groundwater model. A constant average annual recharge value was applied to the groundwater model. This did not allow for studying the response of the model to recharge variability, but was deemed acceptable to account for the tide-induced groundwater fluctuations at base flow and the average geometry of the saltwater-freshwater mixing zone, which have both shown relatively good agreement between model results and observations (Figures 9 and 10). The tidal boundary condition as applied in the numerical model is also subject to inaccuracy. The local tide levels as modeled by POLTIPS-3 software [*National Oceanography Centre*, 2011] were used and therefore model simulations did not account for high frequency sea level variations such as waves or temporary sea level increase due to local wind effects. Also, the topography of the tidal flat computed at an average resolution of 10 m did not permit accounting accurately for sharp topographic variations at dyke locations. Higher-resolution DEM or LIDAR data along with a local sea gauge would be needed for more accurate simulations, particularly for studying the spatiotemporal dynamics of the intertidal saltwater recirculation cell [e.g., *Abarca et al*., 2013] where the model has shown noticeable differences with the ERT results. It is also evident in Figure 11 that the model spatial discretization had an important effect on the thickness of mixing zone between fresh and salt water. This is particularly noticeable at shallow depths (Figure 11a) where in areas of coarser meshing larger numerical dispersion of the mixing zone between fresh and salt water occurs, i.e., in domain areas located at increased distance from the dykes and from the boreholes (Figures 3 and 11). High computational resources would be needed to correct for this by using uniform meshes fine enough to capture the thickness of the dykes (i.e., $\sim$1 m), or dynamic adaptive mesh refinement techniques in areas of steep salinity gradients. Regarding more specifically the model calibration, it has been evidently noticed the high sensitivity of model results (heads and salinities) to the dyke hydraulic conductivity. Storage parameters (storativity and effective porosity) however did not have such an influence on model results. This can be explained by the small volume and low storage values of the dykes compared to the host sandstone, which therefore exerted a higher control. As a result the storativity and effective porosity calibrated in this work are subject to higher uncertainties than the hydraulic conductivities.

The ERT has provided useful information on the saltwater distribution in the aquifer and for the calibration/verification of the groundwater model. The information provided by the resistivity cross sections is however subject to limitations. The apparent resistivities were measured along linear profiles and inverted in 2-D,

which resulted in the influence of lateral heterogeneities (3-D structures) to produce unrealistic distortions within the 2-D cross sections. Similarly, the results of ERT2, which was not undertaken in a straight line in order to follow the high tide level, are subject to possible distortions at increasing depths. Additional resistivity surveys, including 3-D acquisition and inversion would help address the structural distortions and provide a more accurate picture of the saltwater distribution within and across dyke-bounded aquifer units.

A robust petrophysical relationship is key in linking the ERT results with the model calculated salinities. The *Waxman and Smits* [1968] model was used in order to account for the significant amount of clay in the Sherwood sandstone, which the model of *Archie* [1942] cannot. The parametrization of the model was made possible by the large breadth of literature available for the Sherwood sandstone, a major water and energy resource in the UK. Despite having confident regional estimates of Waxman and Smits' parameters (e.g., cementation factor and cation exchange capacity) their actual values and spatial variations at the site were not known and therefore have been assumed homogeneous. The decrease of clay content with depth in the sandstone at the site would result in a decrease in *CEC* which would have to be compensated in the petrophysical model by producing higher pore salinity (i.e., the saltwater mixing zone as interpreted from ERT would appear shallower). Advanced petrophysical studies through specific analysis of surface and borehole samples would be needed for more spatially accurate ERT-modeling comparison.

Ultimately the simulation has provided detailed, high resolution insights on (1) the spatiotemporal effect of low-permeability dykes on flow and salinity patterns and (2) estimates of the hydrogeological properties of the dykes. Specifically, at the study site, the dykes are shown to act as relative barriers to flow and transport. The alteration of both flow and salinity fields is caused by a partial compartmentation of the aquifer with relatively poor groundwater connectivity across dykes resulting in high hydraulic and salinity gradients at dyke locations. Flow paths and head equipotentials tend to orientate respectively parallel and perpendicular to dykes as reported by previous studies of low-permeability dykes [e.g., *Morel and Wikramaratna*, 1982; *Babiker and Gudmundsson*, 2004; *Perrin et al*., 2011]. This results in deviations of heads and salinities from the boundary control exerted by the coastline in homogeneous aquifer systems. These deviations increase with depth, i.e., with distance to the tidal boundary. Freshwater discharge is higher on the land-facing side of the dykes (that receives the land recharge) and saltwater intrusion is enhanced on the sea-facing side of the dykes. On land-facing side of dykes, when compared to a conceptual model without dykes, groundwater heads and depths to saltwater were higher. This is the result of the reduction of the equivalent (upscaled) hydraulic conductivity and transmissivity of the aquifer by the dyke networks, which has been pointed out by previous studies in volcanic settings such as *Takasaki and Mink* [1985] and *Dickson et al*. [2014, 2015]. In average across the study area however, modeled groundwater heads and depth to saltwater were higher in absence of dykes as a result of increased freshwater inflow from upland. The model calibration also provided estimates of flow, storage and transport properties of the dykes. This was assuming dykes as an equivalent porous medium. Fracture flow in individual dyke fractures [*Dickson et al*., 2014] has not been computed and may create quick preferential flow and salt transport across dykes at small (m) scale, therefore reducing salinity contrasts on either side of dykes. Further studies may need to take this into account for more accurate quantifications of dyke hydrogeological properties. Calibrated hydraulic conductivities at the study site have been in average estimated to be in the order of magnitude of 10^{-8} m s^{-1} which is only an order below the values provided by *Perrin et al*. [2011], but the latter authors were investigating partially weathered volcanic dykes in India thus likely to be more permeable. This resulted in contrasts of permeability between dykes and host rock at the site of between 1 and 3 orders of magnitude, the latter being representative to the contrasts of values at the regional scale [*Dickson et al*., 2014, 2015]. Assuming that the order of magnitude obtained for the *K* of the dyke is a good representative of most unweathered dolerite dykes worldwide, one can expect a much higher contrast of *K* in aquifers of higher permeability than the Sherwood sandstone, such as many coastal settings and particularly recent volcanic islands [e.g., *Bourhane et al*., 2016]. Storage parameters for flow (storativity) and transport (effective porosity) for volcanic dykes suffer from a lack of literature values. Despite the low sensitivity of the model to these storage parameters as discussed above, values of about 10^{-3} and 10^{-2} have been obtained for dyke *Sy* and n_e, respectively. These results fall about 1–2 orders of magnitude under the storage properties of the Sherwood sandstone, which are broadly representative of most poorly consolidated sandstones.

This study constitutes the first in situ characterization of the effect of volcanic dykes on saltwater intrusion in a coastal aquifer. While the majority of conceptual representations of dykes in coastal aquifers have been showing them parallel to the coast line [e.g., *Izquierdo*, 2014] defining so-called "dyke-impounded aquifers" and did not

consider their effect on saltwater intrusion, the presented study has investigated an observed cluster of intrusive dykes oriented oblique to the shoreline. The study results show that aquifer units bounded by near-continuous intersecting subvertical dykes favor freshwater accumulation and prevent saltwater intrusion. The results suggest that low-permeability structures as small as 1–2 m wide with a permeability contrast with the surrounding aquifer of at least 1 order of magnitude is sufficient to generate preferential pathways and relative aquifer compartmentalization. However, the study also highlights that beside the contrast in permeability, an important factor for significant freshwater accumulation is the extension (length), angle and continuity of dykes inland, which define the contributing recharge zone (catchment) of the block and therefore the freshwater inflow; the larger the catchment and recharge, the higher the water table, the thicker the freshwater lens and the lower the saltwater intrusion. The role of fractures within dykes, generally perpendicular to dyke orientation, should be investigated in more detail as it may create preferential flow and transport at a smaller (m) scale.

The methodological approach presented demonstrates that saltwater intrusion can be efficiently used as a natural tracer to better characterize groundwater pathways in heterogeneous coastal aquifer systems. The approach also suggest that numerical porous media flow and advective-dispersive transport models can in these conditions be used to realistically simulate flow and solute transport in heterogeneous-discontinuous systems when high resolution verification data sets, such as high frequency groundwater monitoring and high resolution geophysical imaging, are available and integrated. This corroborates the findings by *Dogan et al*. [2015] in highly heterogeneous sedimentary aquifers.

The presented approach can be described as a sequential hydrogeophysical approach (see e.g., discussion in *Herckenrath et al*. [2013a]) where each individual technique of investigation, inversion or modeling (magnetic, ERT inversion, groundwater monitoring and attenuation analysis, numerical analysis) are performed separately. Such a sequential approach has the advantage of individual results to be subject to a geological conceptual interpretation and validation before coupling them with other methods. More quantitative, coupled multiphysics or hydrogeophysical (inverse) modeling frameworks are available and have been to some extent applied to saltwater intrusion problems in relatively homogeneous aquifers [e.g., *Herckenrath et al*., 2013b]. The implementation of coupled inversion for the current case study would allow for more quantitative and integrative sensitivity analysis, including a more accurate quantification as to what extent the geophysical data contribute to the quality of the hydrogeological predictions. Such fully coupled multiphysics approaches are challenging due to the amount of data and computational power required but are promising for complex aquifer systems and potentially a powerful way toward a more quantitative coupling of the diversity of geophysical data involved. Noteworthy, as recently raised by *Linde et al*. [2015], progress in the incorporation of realistic geological conceptual constraints also remain to be made in these fully coupled inversion approaches, particularly for in situ studies of real-world, highly heterogeneous aquifer systems.

More practically, the results provide crucial input data for upscaling aquifer properties to regional scale and the application of models for regional groundwater management. This is exemplified by the recent regional modeling study of the Sherwood sandstone aquifer by *Dickson et al*. [2014, 2015, 2016]. In these studies, observed field-scale hydrodynamic properties of the dykes enabled the estimation of regional properties of dyke clusters of varying densities applied to a 100 km-scale groundwater flow model. As transport was not considered, further research should consider more specifically the upscaling of aquifer transport properties. Yet this demonstrates the applicability of the approach beyond the scale considered in this work. Furthermore, beyond this specific case study, the results provide generalizable insights on in situ preferential flow and transport patterns in other productive aquifers intersected by complex distributions of discrete low-permeability geological features, such as (1) most dyke-intruded volcanic aquifer systems and especially those subject to saltwater intrusion issues, which is a great challenge in volcanic islands and (2) other productive aquifer systems characterized by complex networks of low-permeability geological or artificial features, such as fractured aquifer systems with sealed fractures/faults [e.g., *Bense et al*., 2013], artificial subsurface barriers designed to block (and/or react with) contaminants [e.g., *Naftz et al*., 2002], including saltwater intrusion barriers in coastal aquifers [e.g., *Post*, 2005].

6. Conclusion

This study has provided quantification of the effect of volcanic dykes on groundwater flow and saltwater intrusion at high resolution. An integrated, multiphysics hydrogeological approach was applied and

proved useful to calibrate a three-dimensional numerical groundwater model of a tidal sandstone aquifer in Northern Ireland intersected by a complex network of dolerite dykes. Combining magnetics, resistivity and groundwater monitoring has provided both input (structure and properties) and calibration data sets for the numerical model. The integration of low-permeability dykes, of about 2–3 orders of magnitude lower than the sandstone permeability into the numerical simulations was shown to affect the simulated flow and transport fields. Simulations provided results in good agreement with the field observations and confirm the dykes' role as relative barriers. Specifically, the presence of dykes is responsible for a decrease of hydraulic connectivity between different dyke-bounded aquifer units. Preferential flow path occur parallel to observed dyke orientations. Fresh water inflows from upland recharge areas concentrate on the land-facing side of the dykes and saltwater penetration is higher on the sea-facing side of the dyke. On average (i.e., regionally), the presence of dyke swarms results in a higher water table and larger depth to seawater than in the absence of dykes. It is expected that high-permeability dykes would have an opposed effect in decreasing the water table and enhancing seawater intrusion.

Similar approaches can be applied to a broad range of coastal environments, including contexts with highly conductive structures such as fractures or dissolution patterns. Many coastal settings worldwide, such as volcanic and coral islands are characterized by structurally complex aquifers with high contrasts in their hydrogeological properties. As freshwater resources in these regions are also under great demographic and climatic pressure, understanding, characterizing and modeling the role of heterogeneities such as dykes and fractures is crucial for well-informed sustainable groundwater management. They can also be expanded beyond the scale considered in this work, as well as to a variety of contamination problems involving more or less discrete aquifer heterogeneities.

Further research exploring inverse modeling in fully coupled multiphysics frameworks has a potential to provide more details particularly with regards to the internal heterogeneity/discontinuity of both the dykes and dyke-bounded host sandstone and overcome the conceptual assumptions used when applying the techniques separately and to assist in providing more comprehensive sensitivity and uncertainty analyses.

Appendix A: Tidal Attenuation Analysis—*Jacob* [1950] Analytical Solution

Aquifers located next to tidal bodies are subject to sinusoidal fluctuations in groundwater head due to the rise and fall of tides. The analytical solution of *Jacob* [1950, in *Fetter*, 1994] indicates that head fluctuation (equation (A1)) decreases exponentially with increasing distance from the shoreline, and time lag (equation (A2)) increases linearly with distance. The method considers a vertical beach, straight coastline and one-dimensional flow in a coastal homogenous confined aquifer.

$$H_x = H_0 e^{\left(-x\sqrt{\pi S/t_0 T}\right)} \tag{A1}$$

$$t_{lag} = x\sqrt{t_0 S/4\pi T} \tag{A2}$$

where H_x (m) is the amplitude of the tidal fluctuation at any distance x (m) from the seawater body; H_0 (m) is the amplitude of the tidal change; t_0 (s) is the tidal period; t_{lag} (s) is the time lag of tidal propagation in the aquifer at any distance x; S (no dimension) is the aquifer storativity; and T ($m^2\ s^{-1}$) is the aquifer transmissivity. The solution can also be applied to unconfined flow, as an approximation, if the range of tidal fluctuations is small compared with the saturated aquifer thickness [*Erskine*, 1991].

From equation (A1) the tidal efficiency (TE; no dimension) is defined as H_x/H_0. To obtain a value of diffusivity D ($m^2\ s^{-1}$) defined as T/S, equation (A1) was rearranged resulting in equation (A3):

$$\frac{T}{S} = \frac{\pi x^2}{(\ln TE)^2 t_0} \tag{A3}$$

The time lag t_{lag} is a measure of the speed of propagation of the tidal forcing through the aquifer and is defined as the phase difference between the tidal signal and the well signal. To obtain a diffusivity value, equation (A2) was rearranged to give equation (A4).

$$\frac{T}{S} = \frac{x^2 t_0}{4\pi (t_{lag})^2} \tag{A4}$$

Appendix B: The *Waxman and Smits* [1968] Model

The empirical petrophysical model of *Waxman and Smits* [1968, in *Revil et al.*, 1998] relates the porous media bulk electrical conductivity with the pore water electrical conductivity and the cation exchange capacity of the clay minerals present in the solid matrix. It is expressed as

$$\sigma_{bulk} = \frac{1}{F^*}(\sigma_w + BQ_v) \tag{B1}$$

where $\sigma_{bulk} = {\rho_{bulk}}^{-1}$ is the aquifer bulk conductivity at 25°C (S m^{-1}) and ρ_{bulk} is the aquifer bulk resistivity at 25°C (Ω m); $\sigma_w = {\rho_w}^{-1}$ is the pore water conductivity at 25°C (S m^{-1}), and ρ_w is the pore water conductivity at 25°C (Ω m). The Archie formation factor F^* (no dimension) is expressed as

$$F^* = \frac{1}{ø^m} \tag{B2}$$

where ø is the aquifer porosity (no dimension) and m is the Archie cementation factor (no dimension). The parameter B is the equivalent counterion mobility at 25°C (m^2 s^{-1} V^{-1}) expressed as

$$B = B_0 \left[1 - 0.6e^{\left(-\sigma_w / 0.013\right)}\right] \tag{B3}$$

where $B_0 = 4.78 \times 10^{-8}$ is the max counterion mobility at 25°C (m^2 s^{-1} V^{-1}). Qv is the excess of surface charge per unit pore volume (C m^{-3}; 1 meq $cm^{-3} = 96.32 \times 10^6$ C m^{-3}) expressed as [*Revil et al.*, 1998]:

$$Q_v = \rho_g \left(\frac{1-ø}{ø}\right) CEC \times 96.32 \times 10^6 \tag{B4}$$

where CEC is the cation exchange capacity (meq g^{-1}) and ρ_g is the aquifer grain density (g cm^{-3}).

Equations (B1–B4) were used in this study to determine the pore water conductivity from the bulk resistivity data measured during the ERT surveys. The input bulk conductivity was first converted to 25°C from the formation temperature (T_F in °C), considered uniform and constant in the saturated zone, using the following approximation [*Arps*, 1953]:

$${\sigma_w}^{25°C} = {\sigma_w}^{T_F} \frac{46.5}{T_F + 21.5} \tag{B5}$$

Then finally the total dissolved solids (*TDS*; in kg m^{-3}) were calculated from the calculated pore water conductivity using the simple approximation of *Hem* [1985]:

$$TDS = A \ {\sigma_w}^{25°C} \tag{B6}$$

where the calibration factor (A) is not constant over a wide range of concentrations, but ranges from 0.6 for seawater to 0.5 for fresh or slightly brackish water *Hem* [1985]. A mean value of $A = 0.55$ was used in this work.

Acknowledgments
This research was primarily based on research grant-aided by the Irish Department of Communications, Energy and Natural Resources under the National Geoscience Programme 2007–2013. It also benefited from complementary funding from the Scottish Alliance for Geoscience, Environment and Society (SAGES). We acknowledge the contribution in data acquisition of the MSc students in Environmental Engineering at Queen's University Belfast, the landowner for access to the inland fields and the Department of Geography, Archaeology and Paleoecology at QUB for provision of the tidal model of Belfast Lough. The data used are listed in the references, tables, and figures and are available from the corresponding author upon demand. We acknowledge the constructive comments by the Associate Editor and three reviewers, which helped in improving the final manuscript.

References

Abarca, E., H. Karam, H. F. Hemond, and C. F. Harvey (2013), Transient groundwater dynamics in a coastal aquifer: The effects of tides, the lunar cycle, and the beach profile, *Water Resour. Res.*, *49*, 2473–2488, doi:10.1002/wrcr.20075.

Abdul Nassir, S. S., M. H. Loke, C. Y. Lee, and M. N. M. Nawawi (2000), Salt-water intrusion mapping by geoelectrical imaging surveys, *Geophys. Prospect.*, *48*(4), 647–661, doi:10.1046/j.1365-2478.2000.00209.x.

Archie, G. E. (1942), The electrical resistivity log as an aid in determining some reservoir characteristics, *Trans. Am. Inst. Min. Metall. Pet. Eng.*, *146*(1), 54–62, doi:10.2118/942054-G.

Arps, J. J. (1953), The effect of temperature on the density and electrical resistivity of sodium chloride solutions, *J. Pet. Technol.*, *5*(10), 17–20, doi:10.2118/953327-G.

Attwa, M., T. Günther, M. Grinat, and F. Binot (2011), Evaluation of DC, FDEM and IP resistivity methods for imaging perched saltwater and a shallow channel within coastal tidal flat sediments, *J. Appl. Geophys.*, *75*(4), 656–670, doi:10.1016/j.jappgeo.2011.09.002.

Babiker, M., and A. Gudmundsson (2004), The effects of dykes and faults on groundwater flow in an arid land: The Red Sea Hills, Sudan, *J. Hydrol.*, *297*(1), 256–273, doi:10.1016/j.jhydrol.2004.04.018.

Ball, D., P. McConvey, and E. Campbell (2005), *A Groundwater Vulnerability Screening Methodology for Northern Ireland*, Br. Geol. Surv., Keyworth, Nottingham, U. K.

Bear, J., A. H. D. Cheng, S. Sorek, D. Ouazar, and I. Herrera (eds.) (1999), *Seawater Intrusion in Coastal Aquifers: Concepts, Methods and Practices*, vol. 14, Springer, Netherlands. [Avaiable at http://www.springer.com/gb/book/9780792355731.]

Beaujean, J., F. Nguyen, A. Kemna, A. Antonsson, and P. Engesgaard (2014), Calibration of seawater intrusion models: Inverse parameter estimation using surface electrical resistivity tomography and borehole data, *Water Resour. Res.*, *50*, 6828–6849, doi:10.1002/2013WR014020.

Bennett, J. R. P. (1976), The Lagan Valley: Hydrogeological study, *Open File Rep. 57*, Geol. Surv. of North. Ireland, Belfast.

Bense, V. F., T. Gleeson, S. E. Loveless, O. Bour, and J. Scibek (2013), Fault zone hydrogeology, *Earth Sci. Rev.*, *127*, 171–192, doi:10.1016/j.earscirev.2013.09.008.

Berkowitz, B. (2002), Characterizing flow and transport in fractured geological media: A review, *Adv. Water Resour.*, *25*(8), 861–884.

Boehmer, W. K., and J. Boonstra (1987), Analysis of drawdown in the country rock of composite dike aquifers, *J. Hydrol.*, *94*(3), 199–214, doi:10.1016/0022-1694(87)90053-9.

Boonstra, J., and W. K. Boehmer (1986), Analysis of data from aquifer and well tests in intrusive dikes, *J. Hydrol.*, *88*(3), 301–317, doi:10.1016/0022-1694(86)90096-X.

Bourhane, A., J.-C. Comte, J.-L. Join, and K. Ibrahim (2016), Groundwater prospection in Grande Comore Island—Joint contribution of geophysical methods, hydrogeological time-series analysis and groundwater modelling, in *Active Volcanoes of the Southwest Indian Ocean*, edited by P. Bachelery et al., pp. 385–401, Springer, Berlin, doi:10.1007/978-3-642-31395-0_24.

Bouwer, H., and R. C. Rice (1976), A slug test for determining hydraulic conductivity of unconfined aquifers with completely or partially penetrating wells, *Water Resour. Res.*, *12*(3), 423–428, doi:10.1029/WR012i003p00423.

Bromley, J., B. Mannström, D. Nisca, and A. Jamtlid (1994), Airborne geophysics: Application to a ground-water study in Botswana, *Ground Water*, *32*(1), 79–90, doi:10.1111/j.1745-6584.1994.tb00614.x.

Carrera, J., J. J. Hidalgo, L. J. Slooten, and E. Vázquez-Suñé (2010), Computational and conceptual issues in the calibration of seawater intrusion models, *Hydrogeol. J.*, *18*(1), 131–145.

Chacksfield, B. C. (2010), A preliminary interpretation of Tellus airborne magnetic and electromagnetic data for Northern Ireland, *Br. Geol. Surv. Internal Rep. IR/07/041*, Br. Geol. Surv., Nottingham, U. K.

Comte, J.-C., and O. Banton (2007), Cross-validation of geo-electrical and hydrogeological models to evaluate seawater intrusion in coastal aquifers, *Geophys. Res. Lett.*, *34*, L10402, doi:10.1029/2007GL029981.

Comte, J.-C., O. Banton, J.-L. Join, and G. Cabioch (2010), Evaluation of effective groundwater recharge of freshwater lens in small islands by the combined modeling of geoelectrical data and water heads, *Water Resour. Res.*, *46*, W06601, doi:10.1029/2009WR008058.

Comte, J.-C., J.-L. Join, O. Banton, and E. Nicolini (2014), Modelling the response of fresh groundwater to climate and vegetation changes in coral islands, *Hydrogeol. J.*, *22*(8), 1905–1920, doi:10.1007/s10040-014-1160-y.

Cook, P. G. (2003), *A Guide to Regional Groundwater Flow in Fractured Rock Aquifers*, CSIRO Land and Water, Glen Osmond, Australia.

Cooper, H. H., and C. E. Jacob (1946), A generalized graphical method for evaluating formation constants and summarizing well-field history, *Trans. AGU*, *27*(4), 526–534.

Cooper, M. R., H. Anderson, J. J. Walsh, C. L. Van Dam, M. E. Young, G. Earls, and A. Walker (2012), Palaoegene Alpine tectonics and Icelandic plume-related magmatism and deformation in Northern Ireland, *J. Geol. Soc.*, *169*(1), 29–36, doi:10.1144/0016-76492010-182.

Cronin, A. A., J. A. C. Barth, T. Elliot, and R. M. Kalin (2005), Recharge velocity and geochemical evolution for the Permo-Triassic Sherwood sandstone, Northern Ireland, *J. Hydrol.*, *315*(1), 308–324, doi:10.1016/j.jhydrol.2005.04.016.

Custodio, E. (2007), Groundwater in volcanic hard rocks, in *Groundwater in Fractured Rocks, IAH Selec. Pap. Ser.*, vol. 9, edited by J. Krásný and J. M. Sharp Jr., pp. 95–108, Taylor and Francis, London, doi:10.1201/9780203945650.ch5.

De Marsily, G., F. Delay, J. Goncalves, P. Renard, V. Teles, and S. Violette, S. (2005). Dealing with spatial heterogeneity, *Hydrogeol. J.*, *13*(1), 161–183.

Dickson, N., J.-C. Comte, J. McKinley, and U. Ofterdinger (2016), The use of aero-magnetics to enhance a numerical groundwater model of the Lagan Valley aquifer, Northern Ireland, in *Unearthed: Impacts of the Tellus Surveys of the North of Ireland, R. Irish Acad.: Sci. Ser.*, edited by M. Young, R. Irish Acad., Dublin, doi:10.3318/978-1-908996-88-6.CH28.

Dickson, N. E. M., J.-C. Comte, J. McKinley, and U. Ofterdinger (2014), Coupling ground and airborne geophysical data with upscaling techniques for regional groundwater modeling of heterogeneous aquifers: Case study of a sedimentary aquifer intruded by volcanic dykes in Northern Ireland, *Water Resour. Res.*, *50*, 7984–8001, doi:10.1002/2014WR015320.

Dickson, N. E. M., J.-C. Comte, P. Renard, J. A. Straubhaar, J. M. McKinley, and U. Ofterdinger (2015), Integrating aerial geophysical data in multiple-point statistics simulations to assist groundwater flow models, *Hydrogeol. J.*, *23*(5), 883–900, doi:10.1007/s10040-015-1258-x.

Dogan, M., R. L. Van Dam, G. Liu, M. M. Meerschaert, J. J. Butler Jr., G. C. Bohling, D. A. Benson, and D. W. Hyndman (2014), Predicting flow and transport in highly heterogeneous alluvial aquifers, *Geophys. Res. Lett.*, *41*, 7560–7565, doi:10.1002/2014GL061800.

Earls, G., and M. Young (2010), North American liaisons, *Earthwise*, *26*, 16–17.

Engel, R., D. J. McFarlane, and G. Street (1987), The influence of dolerite dykes on saline seeps in southwestern Australia, *Soil Res.*, *25*(2), 125–136, doi:10.1071/SR9870125.

Engel, R., D. J. McFarlane, and G. J. Street (1989), Using geophysics to define recharge and discharge areas associated with saline seeps in south-western Australia, in *Groundwater Recharge*, edited by M. L. Sharma, pp. 25–39, A. A. Balkema, Rotterdam, Netherlands.

Ernst, R. E. (2014), *Large Igneous Provinces*, Cambridge Univ. Press, Cambridge, U. K.

Erskine, A. D. (1991), The effect of tidal fluctuation on a coastal aquifer in the UK, *Ground Water*, *29*(4), 556–562, doi:10.1111/j.1745-6584.1991.tb00547.x.

European Commission (2006), DIRECTIVE 2006/118/EC on the protection of groundwater against pollution and deterioration, *Off. J. Eur. Union*, 19–31.

Fetter, C.W. (1994), *Applied Hydrogeology*, 3rd ed., 616 pp., Macmillan, New York.

Günther, T., C. Rücker, and K. Spitzer (2006), Three-dimensional modelling and inversion of DC resistivity data incorporating topography—II. Inversion, *Geophys. J. Int.*, *166*(2), 506–517, doi:10.1111/j.1365-246X.2006.03011.x.

Hartley, J. J. (1935), *The Underground Water Resources of Northern Ireland*, Inst. of Civ. Eng. (North. Ireland Assoc.), Belfast.

Healy, R. W., and P. G. Cook (2002), Using groundwater levels to estimate recharge, *Hydrogeol. J.*, *10*(1), 91–109, doi:10.1007/s10040-001-0178-0.

Hem, J. D. (1985), *Study and Interpretation of the Chemical Characteristics of Natural Water*, vol. 2254, Dep. of the Inter., U.S. Geol. Surv., Alexandria, Va.

Herckenrath, D., G. Fiandaca, E. Auken, and P. Bauer-Gottwein (2013a), Sequential and joint hydrogeophysical inversion using a field-scale groundwater model with ERT and TDEM data, *Hydrol. Earth Syst. Sci.*, *17*(10), 4043–4060, doi:10.5194/hess-17-4043-2013.
Herckenrath, D., N. Odlum, V. Nenna, R. Knight, E. Auken, and P. Bauer-Gottwein (2013b), Calibrating a Salt Water Intrusion Model with time-domain electromagnetic data, *Ground Water*, *51*(3), 385–397, doi:10.1111/j.1745-6584.2012.00974.x.
Izquierdo, T. (2014) Conceptual hydrogeological model and aquifer system classification of a small volcanic island (La Gomera; Canary Islands), *Catena*, *114*, 119–128, doi:10.1016/j.catena.2013.11.006.
Jacob, C. E. (1950), Flow of groundwater, in *Engineering Hydraulics*, edited by H. Rouse, pp. 321–386, John Wiley, New York.
Kalin, R. M., and C. Roberts (1997), Groundwater resources in the Lagan Valley sandstone aquifer, Northern Ireland, *Water Environ. J.*, *11*(2), 133–139, doi:10.1111/j.1747-6593.1997.tb00104.x.
Kirkegaard, C., T. O. Sonnenborg, E. Auken, and F. Jørgensen (2011), Salinity distribution in heterogeneous coastal aquifers mapped by airborne electromagnetics, *Vadose Zone J.*, *10*(1), 125–135, doi:10.2136/vzj2010.0038.
Koukadaki, M. A., G. P. Karatzas, M. P. Papadopoulou, and A. Vafidis (2007), Identification of the saline zone in a coastal aquifer using electrical tomography data and simulation, *Water Resour. Manage.*, *21*(11), 1881–1898, doi:10.1007/s11269-006-9135-y.
Lewis, M. F. (1991), Lineaments and salinity in Western Australia: Carriers or barriers?, in *National Conference Publication—Institute of Engineers, Australia*, vol. 1, no. 91, pp. 202–209.
Linde, N., P. Renard, T. Mukerji, and J. Caers (2015), Geological realism in hydrogeological and geophysical inverse modeling: A review, *Adv. Water Resour.*, *86*, 86–101, doi:10.1016/j.advwatres.2015.09.019.
MAG3D (2006), *A Program Library for Forward Modelling and Inversion of Magnetic Data over 3D Structures, Version 4.0*, UBC-Geophys. Inversion Facil., Dep. of Earth and Ocean Sci., Univ. of B. C., Vancouver, Canada.
McKinley, J. M., R. H. Worden, and A. H. Ruffell (2001), Contact diagenesis: The effect of an intrusion on reservoir quality in the Triassic Sherwood Sandstone Group, Northern Ireland, *J. Sediment. Res.*, *71*(3), 484–495, doi:10.1306/2DC40957-0E47-11D7-8643000102C1865D.
McNeill, G. W., A. A. Cronin, Y. Yang, T. Elliot, and R. M. Kalin (2000), The Triassic Sherwood Sandstone Aquifer in Northern Ireland: Constraint of a groundwater flow model for resource management, in *Groundwater in the Celtic Regions: Studies in Hard Rock and Quaternary Hydrogeology*, edited by N. S. Robins and B. D. Misstear, *Geol. Soc. Spec. Publ.*, 182, 179–190.
Mitchell, W. I. (2004), Triassic, in *The Geology of Northern Ireland; Our Natural Foundation*, 2nd ed., edited by W. I. Mitchell, pp. 133–144, Geol. Surv. of North. Ireland, Belfast.
Moench, A. F. (1995), Combining the Neuman and Boulton models for flow to a well in an unconfined aquifer, *Ground Water*, *33*(3), 378–384.
Moench, A. F. (1997), Flow to a well of finite diameter in a homogeneous, anisotropic water table aquifer, *Water Resour. Res.*, *33*(6), 1397–1407, doi:10.1029/97WR00651.
Morel, E. H., and R. S. Wikramaratna (1982), Numerical modelling of groundwater flow in regional aquifers dissected by dykes, *Hydrol. Sci. J.*, *27*(1), 63–77, doi:10.1080/02626668209491086.
Naftz, D., S. J. Morrison, C. C. Fuller, and J. A. Davis (eds.) (2002), *Handbook of Groundwater Remediation Using Permeable Reactive Barriers: Applications to Radionuclides, Trace Metals, and Nutrients*, Academic Press, San Diego, Calif.
National Oceanography Centre (2011), *POLTIPS-3*, Liverpool, U. K.
Neuman, S. P. (2005), Trends, prospects and challenges in quantifying flow and transport through fractured rocks, *Hydrogeol. J.*, *13*(1), 124–147.
Nguyen, F., A. Kemna, A. Antonsson, P. Engesgaard, O. Kuras, R. Ogilvy, J. Gisbert, S. Jorreto, and A. Pulido-Bosch (2009), Characterization of seawater intrusion using 2D electrical imaging, *Near Surface Geophys*, *7*(5–6), 377–390, doi:10.3997/1873-0604.2009025.
Oldenburg, D. W., and Y. Li (1999), Estimating depth of investigation in dc resistivity and IP surveys, *Geophysics*, *64*(2), 403–416, doi:10.1190/1.1444545.
Palacky, G. J. (1988), Resistivity characteristics of geologic targets, in *Electromagnetic Methods in Applied Geophysics: Application (2 vols.)*, edited by M. N. Nabighian, pp. 53–129, Soc. of Expl. Geophys., Tulsa, Okla.
Parasnis, D. S. (2012), *Principles of Applied Geophysics*, Springer, Netherlands.
Perrin, J., S. Ahmed, and D. Hunkeler (2011), The effects of geological heterogeneities and piezometric fluctuations on groundwater flow and chemistry in a hard-rock aquifer, southern India, *Hydrogeol. J.*, *19*(6), 1189–1201, doi:10.1007/s10040-011-0745-y.
Post, V. E. A. (2005), Fresh and saline groundwater interaction in coastal aquifers: Is our technology ready for the problems ahead?, *Hydrogeol. J.*, *13*(1), 120–123, doi:10.1007/s10040-004-0417-2.
Revil, A., L. M. Cathles III, S. Losh, and J. A. Nunn (1998), Electrical conductivity in shaly sands with geophysical applications, *J. Geophys. Res.*, *103*(B10), 23,925–23,936, doi:10.1029/98JB02125.
Robins, N. S. (1996), *Hydrogeology of Northern Ireland*, Environ. and Heritage Serv., HMSO for the Br. Geol. Soc. London, London.
Rücker, C., T. Günther, and K. Spitzer (2006), Three-dimensional modelling and inversion of DC resistivity data incorporating topography—I. Modelling, *Geophys. J. Int.*, *166*(2), 495–505, doi:10.1111/j.1365-246X.2006.03010.x.
Sami, K., and D. A. Hughes (1996), A comparison of recharge estimates to a fractured sedimentary aquifer in South Africa from a chloride mass balance and an integrated surface-subsurface model, *J. Hydrol.*, *179*(1), 111–136, doi:10.1016/0022-1694(95)02843-9.
Si, H. (2008), *TetGen—A Quality-Constrained Tetrahedral Mesh Generator*, Weierstrass Inst., Berlin. [Available at http://www.tetgen.org.]
Simmons, C. T., T. R. Fenstemaker, and J. M. Sharp (2001), Variable-density groundwater flow and solute transport in heterogeneous porous media: Approaches, resolutions and future challenges, *J. Contam. Hydrol.*, *52*(1), 245–275.
Singhal, B. B. S., and R. P. Gupta (1999), *Applied Hydrogeology of Fractured Rocks*, 400 pp., Kluwer, Dordrecht, Netherlands.
Souza, W. R., and C. I. Voss (1987), Analysis of an anisotropic coastal aquifer system using variable-density flow and solute transport simulation, *J. Hydrol.*, *92*(1–2), 17–41.
Sultan, M., A. Wagdy, N. Manocha, W. Sauck, K. Abdel Gelil, A. F. Youssef, R. Becker, A. Milewski, Z. El Alfy, and C. Jones (2008), An integrated approach for identifying aquifers in transcurrent fault systems: The Najd shear system of the Arabian Nubian shield, *J. Hydrol.*, *349*(3–4), 475–488, doi:10.1016/j.jhydrol.2007.11.029.[10.1016/j.jhydrol.2007.11.029]
Summer, N. S., and S. Ayalon (1995) Dike intrusion into unconsolidated sandstone and the development of quartzite contact zones, *J. Struct. Geol.*, *17*(7), 997–1010.
Takasaki, K. J., and J. F. Mink (1985), Evaluation of major dike-impounded ground-water reservoirs, Island of Oahu, *U.S. Geol. Surv. Water Supply Pap.*, *2217*, 85 p.
Taylor, S., and R. Barker (2006), Modelling the DC electrical response of fully and partially saturated Permo-Triassics sandstone, *Geophys. Prospect.*, *54*(3), 351–367, doi:10.1111/j.1365-2478.2006.00538.x.
Van Dam, R. L., B. P. Eustice, D. W. Hyndman, W. W. Wood, and C. T. Simmons (2014), Electrical imaging and fluid modeling of convective fingering in a shallow water-table aquifer, *Water Resour. Res.*, *50*, 954–968, doi:10.1002/2013WR013673.

Vittecoq, B., J. Deparis, S. Violette, T. Jaouen, and F. Lacquement (2014), Influence of successive phases of volcanic construction and erosion on Mayotte Island's hydrogeological functioning as determined from a helicopter-borne resistivity survey correlated with borehole geological and permeability data, *J. Hydrol.*, *509*, 519–538, doi:10.1016/j.jhydrol.2013.11.062.

Vittecoq, B., P. A. Reninger, S. Violette, G. Martelet, B. Dewandel, and J. C. Audru (2015), Heterogeneity of hydrodynamic properties and groundwater circulation of a coastal andesitic volcanic aquifer controlled by tectonic induced faults and rock fracturing—Martinique Island (Lesser Antilles—FWI), *J. Hydrol.*, *529*, 1041–1059, doi:10.1016/j.jhydrol.2015.09.022.

Waxman, M. H., and L. J. M. Smits (1968), Electrical conductivities in oil-bearing shaly sands, *Soc. Pet. Eng.*, *8*(2), 107–122.

Werner, A. D., M. Bakker, V. E. Post, A. Vandenbohede, C. Lu, B. Ataie-Ashtiani, C. T. Simmons, and D. A. Barry (2013), Seawater intrusion processes, investigation and management: Recent advances and future challenges, *Adv. Water Resour.*, *51*, 3–26, doi:10.1016/j.advwatres.2012.03.004.

Wilkes, S. M., T. P. Clement, and C. J. Otto (2004), Characterisation of the hydrogeology of the Augustus River catchment, Western Australia, *Hydrogeol. J.*, *12*(2), 209–223, doi:10.1007/s10040-003-0298-9.

Williams, J. A., and R. L. Soroos (1973), Evaluation of methods of pumping test analyses for application to Hawaiian aquifers, *Tech. Rep. 70*, 159 pp., Water Resour. Res. Cent., Univ. of Hawaii, Honolulu.

Yang, Y. S., A. A. Cronin, T. Elliot, and R. M. Kalin (2004), Characterizing a heterogeneous hydrogeological system using groundwater flow and geochemical modelling, *J. Hydraul. Res.*, *42*(S1), 147–155, doi:10.1080/00221680409500058.

Young, M. (Eds.) (2016), *Unearthed: Impacts of the Tellus Surveys of the North of Ireland, Science Series*, 440 p., R. Irish Acad., Dublin.

Zheng, C., and S. M. Gorelick (2003), Analysis of solute transport in flow fields influenced by preferential flowpaths at the decimeter scale, *Ground Water*, *41*(2), 142–155.